

Classification mapping of salt marsh vegetation by flexible monthly NDVI time-series using Landsat imagery

Chao Sun^{a,b,*1}, Sergio Fagherazzi^b, Yongxue Liu^{c,**}

^a Department of Geography & Spatial Information Techniques, Ningbo University, Ningbo, Zhejiang Province, China

^b Department of Earth and Environment, Boston University, Boston, MA, USA

^c Department of Geographic Information Science, Nanjing University, Nanjing, Jiangsu Province, China



ARTICLE INFO

Keywords:

Salt marsh vegetation community
Classification mapping
Long-term monitoring
Remote sensing time-series
C5.0 decision tree
Landsat imagery

ABSTRACT

Salt marshes are deemed as one of the most dynamic and valuable ecosystems on Earth. Recently, salt marsh deterioration and loss have become widespread because of anthropogenic stressors and sea level rise. Long-term acquisition of spatial information on salt marsh vegetation communities is thus critical to detect the general evolutionary trend of marsh ecosystems before irreversible change occurs. Medium resolution imagery organized in inter-annual time series has been proven suitable for large-scale mapping of salt marsh vegetation. For long-term monitoring purpose, the challenge still lies in developing time series based on data with sparse and uneven temporal distribution. This paper proposes a flexible Monthly NDVI Time-Series (MNTS) approach to achieve multi-temporal classification maps of salt marsh vegetation communities in the Virginia Coast Reserve, USA, by utilizing all viable Landsat TM/ETM + images during the period 1984–2011. Salt marsh vegetation communities are identified on a reference MNTS spanning 12 months with an overall accuracy of 0.898, approximately 0.107 higher than classifications using single images. Utilizing a flexible selection process based on the reference MNTS, a significant inverse hyperbolic relationship emerges between overall accuracy and average length of the time series. Based on these results, eight classification maps with average accuracy of 0.844 and time interval of 2–5 years are acquired. A spatio-temporal analysis of the maps indicates that the upper low marsh vegetation community has diminished by 19.4% in the study period, with a recent acceleration of losses. The conversion of marsh area to vegetation communities typical of low elevations (37.7 km^2) is more than twice the conversion to vegetation communities typical of high elevations (18.3 km^2), suggesting that salt marsh ecosystems at the Virginia Coast Reserve are affected by sea level rise.

1. Introduction

Salt marshes are highly productive ecosystems, providing an array of ecosystem services (Costanza et al., 1997; Gedan et al., 2009; Zedler and Kercher, 2005). At a local scale, salt marshes play an important role in food supply, nutrient cycling, contaminant filter, sediment storage, and flood control. At a broader scale, salt marshes help regulate regional climate and provide critical habitat for continental and intercontinental migratory species (Zedler and Kercher, 2005). Despite these important benefits, a significant fraction of salt marshes has been lost due to land development, filling and dredging, or damaged by anthropogenic modifications (Gedan et al., 2009). Sea level rise has also a significant impact on the condition and health of coastal salt marshes, especially for those with a limited sediment supply (Morris et al., 2002).

Salt marsh halophytic vegetation is composed of communities adapted to survive different submersion periods. As a result, the distribution of plant communities is usually a function of salt marsh elevation relative to sea level (Isacch et al., 2006; Lenssen et al., 1999; Silvestri et al., 2005). In fact, the interactions between flooding regime, local topography, and ecophysiological performance may result in a diversification of vegetation species along inundation gradients (Boutin and Keddy, 1993; Isacch et al., 2006; Silvestri et al., 2005). This diversification, at the landscape level, is often represented as belt-shaped vegetation type communities around channels and ponds, where the land is higher. Thus, as sea level rises, these communities might transgress landward toward higher areas or disappear altogether if inland marsh expansion is impossible.

As a countermeasure to increasing natural and anthropogenic

* Corresponding author. Ningbo University, Ningbo, Zhejiang Province, 315211, China.

** Corresponding author. Nanjing University, Nanjing, Jiangsu Province, 210023, PR China.

E-mail addresses: sunchaonju@yeah.net (C. Sun), sergio@bu.edu (S. Fagherazzi), yongxue@nju.edu.cn (Y. Liu).

¹ Visiting scholar at Boston University, Boston, MA, 02215, USA.

pressures, acquisition of long-term information on spatial distribution of salt marsh vegetation communities is urgently important, and will help to develop effective strategies for salt marsh management, protection, and restoration (Belluco et al., 2006; Harvey and Hill, 2001; Silvestri et al., 2005). Compared to expensive field measurements in areas with low accessibility, remote sensing has outstanding advantages in its synoptic coverage and repeatability. In terms of classification of salt marsh communities or species by a remotely sensed approach, most studies focused on the usage of high spatial or high spectral (hyperspectral) imagery by either reducing spectral mixing effects in smaller pixels or increasing discriminative capability in a high-dimensional features space (Bachmann et al., 2003; Gilmore et al., 2008; Laba et al., 2008; Timm and McGarigal, 2012; Whiteside and Bartolo, 2015). The high discrimination capabilities demonstrated through the usage of high resolution spatial and hyperspectral data is in turn balanced by their relatively high cost and low availability, which relegate salt marsh monitoring to small regions and few temporal snapshots. Multispectral imagery at medium spatial resolution is an alternative option for salt marsh monitoring applications. These sensors can cover a wide geographic area, have a high temporal depth of the archive, and are freely available. However, high similarity in the spectral signatures of various vegetation species leads to low accuracies for vegetation classification based on a single image, even at the community level (Harvey and Hill, 2001; Klemas, 2013). One example is NOAA Coastal Change Analysis Program (C-CAP), which employs individual Landsat images as primary data to produce classification maps for coastal land cover spanning 25 vegetation categories. However, C-CAP regards the whole coastal salt marsh area as a unique class named Estuarine Emergent Wetland (Fig. 1a).

Recently, significant spectral Vegetation Indices (VIs) have been derived from field spectral observations at different monthly resolutions (Feilhauer et al., 2013; Fernandes et al., 2013; Gao and Zhang, 2006). This raises the possibility of accurate discrimination of salt marsh vegetation communities by means of VIs time-series constructed from multispectral, medium-resolution imagery. Good results have been achieved through time-series spanning 1–3 years with a combination of different VIs (e.g., NDVI, NDAVI, WVI, WAVI) and time scales (e.g., seasonal, monthly in the growing season or the whole year) (Davranche et al., 2010; Gilmore et al., 2008; Sun et al., 2016; Villa et al., 2015; Wang et al., 2012). Among VIs, the Normalized Difference Vegetation Index (NDVI) is accepted as a stable general indicator of community type, plant biomass, vegetation phenology, and photosynthetic performance of salt marsh vegetation (Kerr and Ostrovsky, 2003; Shao et al., 2016; Sun et al., 2016). Neither as spectrally powerful as hyperspectral nor as spatially detailed as high-spatial resolution imagery, a multispectral medium-resolution vegetation mapping with NDVI time-series can go beyond the local scale and short time intervals providing long-term earth observations (Jakimow et al., 2017; la Cecilia et al., 2016; Li et al., 2017; Sun et al., 2017; Zhao et al., 2016). However, the reduced number of useful images should be considered before applications, since the difference between total images and viable images becomes large in coastal zones, where salt marsh vegetation communities grow. Here, the frequent cloud cover and the fluctuating tidal stage lead to a reduced number of viable images with an uneven and discrete temporal distribution. How to synthesize information from these irregular time series of images is therefore critical for the long-term monitoring of salt marshes.

In this study, we explore a new approach to monitor salt marsh vegetation communities with Landsat TM/ETM + multispectral remote sensing data. Our goal is to determine the evolution of marsh vegetation at the Virginia Coast Reserve (VCR), USA, through a series of classification maps spanning 30 years. Salt marsh vegetation communities are classified with the C5.0 decision tree. Our specific objectives are: (1) to construct a reference monthly NDVI time-series (MNTS) spanning 12 months for vegetation classification and compare its performance with classifications based on single images from each month; (2) to generate

a series of classification maps balancing accuracy with frequency, using a flexible MNTS approach acting on all viable Landsat TM/ETM + imagery during 1984–2011; (3) based on the classification maps of salt marsh vegetation communities, to explore spatio-temporal variations in salt marsh communities and determine trends in vegetation cover within the salt marshes of the VCR.

2. Materials

2.1. Study area

The Virginia Coast Reserve (VCR) is a typical barrier-lagoon-marsh system located on the Atlantic side of the Delmarva Peninsula, USA. These lagoons comprise intertidal and subtidal basins located between the barrier islands and the Delmarva Peninsula (Fig. 1a). Tides are semidiurnal, with a mean tidal range of 1.2 m. Mean Higher High Water (MHHW) at Wachapreague channel (NOAA station 8631044, Fig. 1a) is 0.68 m above mean sea level, whereas Mean Lower Low Water (MLLW) is –0.65 m. Marsh vegetation is dominated by *Spartina alterniflora* (*S. alterniflora*), with a height ranging between 50 and 100 cm.

2.2. Definition of salt marsh vegetation communities

To define salt marsh vegetation communities, we start from the mapping units proposed by McCaffrey and Dueser (1990) for hydric-halophytic herbaceous vegetation at the VCR. This classification system, derived from the interpretation of 1:20000-scale false color aerial images and field surveys, delineates mapping units based on species composition, growth form, leaf and stem density, tidal influence, and distinct vertical elevation. The classification has been widely accepted with slight modification for salt marshes across the eastern shore of the United States (McCarthy and Halls, 2014; Pengra et al., 2007; Timm and McGarigal, 2012). However, narrow ecotones and small vegetation patches were undetectable at the medium spatial resolution of Landsat images used in our study. We therefore combined several adjacent mapping units of McCaffrey and Dueser (1990). The final definition of each salt marsh vegetation community used herein is (Fig. 2):

Low Marsh (LM). LM has 75%–100% cover of *S. alterniflora*, often interspersed with *Salicornia virginica* (*S. virginica*). Higher elevations in LM usually have firm organic sediments and support short, often dense, *S. alterniflora*. Lower elevations have fine-grained, mucky sediments which are inundated several hours per day supporting tall *S. alterniflora*.

Upper Low Marsh (ULM). A halophytic association (50–100% cover), usually flooded to a depth of <10 cm, occupies the higher elevations of the LM. It is dominated by *S. virginica* and short *S. alterniflora*, often with a belt of *Distichlis spicata* (*D. spicata*).

High Marsh (HM). HM has 100% cover of dense, typically decumbent, *D. spicata*, *Spartina patens* (*S. patens*) and *Juncus roemerianus* (*J. roemerianus*) with numerous salty-to-brackish ponds. This association fringes the edges of salt flats. Due to the range of salinity, HM may gradually merge with ULM shoreward or dense grassland and shrubs landward.

Tidal Flat (TF). consists of salt flats, mud flats, wash flats, and open water. Salt flats are intermittently flooded areas with a high salt concentration, often covered with a surface layer of unicellular algae and sulfur bacteria. Mud flats have a muddy surface, and are usually devoided of vegetation except for occasional *Ulva lactuca*, *S. alterniflora* and other halophytes. Wash flats appear as bayshore beaches, and bury LM in overwash areas and in ephemeral inlets. Open water comprises ephemeral or permanent ponds, tidal creeks, and the bays in general.

2.3. Data set

2.3.1. Remote sensing data

The remote sensing data used in our study include Landsat imagery,

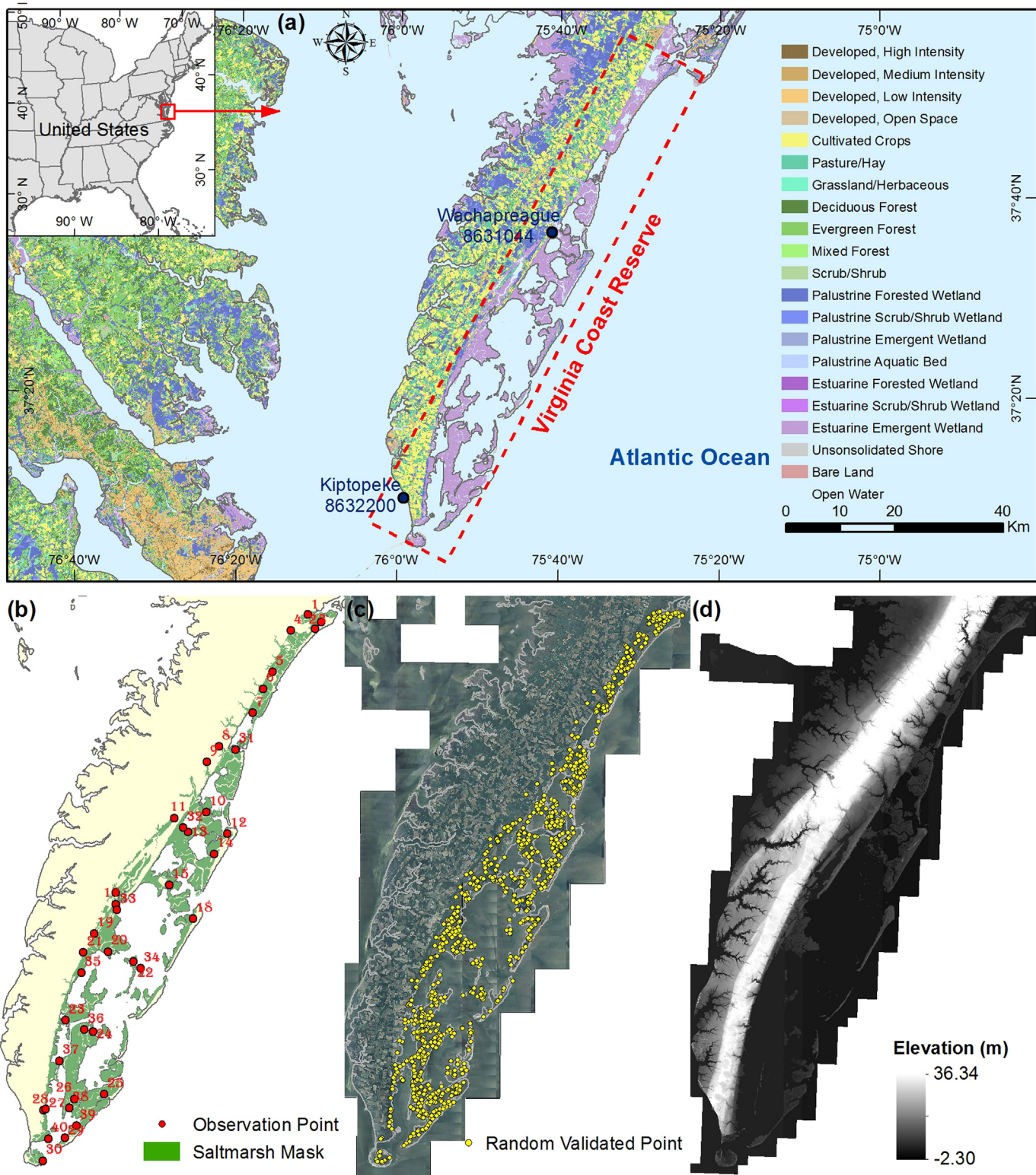


Fig. 1. Study location and available datasets for the Virginia Coast Reserve (VCR). (a) NOAA C-CAP land cover map of 2010; (b) extent of salt marsh area and distribution of available field data; (c) NAIP aerial image of 2004 and distribution of 1000 random validation points; (d) LiDAR-derived DEM of 2010.

NAIP aerial imagery, C-CAP land cover maps, and a LiDAR-derived DEM.

Landsat-5 TM data provide nearly continuous coverage of the earth surface from 1984 to 2011 at a spatial resolution of 30 m. Landsat-7 ETM + SLC-on data (1999–2003), with similar spectral distribution and same spatial resolution is an efficient way to enhance the imagery

availability. The images from 1984 to 2011 for a Landsat scene centered over the VCR (Path: 014, Row: 034) were acquired from the United States Geological Survey (USGS) Earth Explorer and were used for the construction of Monthly NDVI Time-Series (MNTS).

NOAA Coastal Change Analysis Program (C-CAP) maps cover intertidal areas, wetlands, and adjacent uplands. These maps include 25

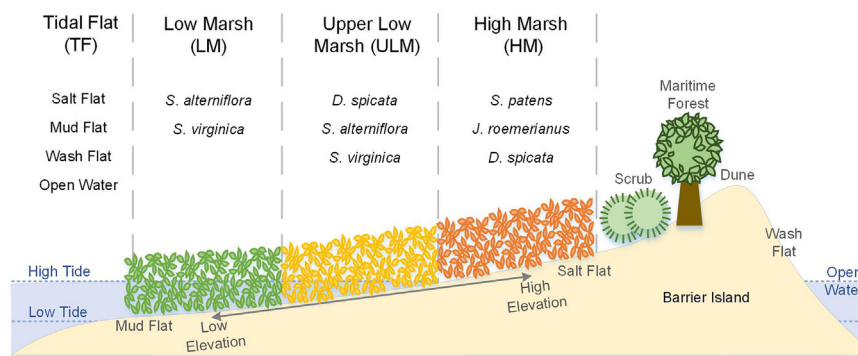


Fig. 2. Vertical distribution and dominant species for salt marsh vegetation communities in our classification system.

land use and vegetation classes with the spatial resolution of 30 m and are updated every five years starting in 1992. In total, 5 C-CAP land cover maps were obtained from NOAA office for coastal management, for the years 1992, 1996, 2001, 2006, and 2010. In the C-CAP classification system, the whole salt marsh area of the VCR was categorized into a unique class labeled Estuarine Emergent Wetland. Thus, the maximum extent of this class from each period was used to delimit the salt marsh region of our study (Fig. 1b).

The National Agriculture Imagery Program (NAIP) acquires aerial imagery at a resolution of 1 m for the United States during the agricultural growing season. A total of 6 NAIP county mosaic images were collected from the United States Department of Agriculture (USDA) Geospatial Data Gateway for the years 2004, 2005, 2006, 2008, 2009, and 2011 (Fig. 1c). Afterwards, 1000 random points were generated with the assistance of ArcGIS software (Foody, 2002a; Theobald et al., 2007) and labeled with salt marsh vegetation classes by interpreting the NAIP images. These points were further utilized for accuracy assessment of classification maps during 2002–2011 as testing samples (Fig. 1c).

A LiDAR-derived DEM of the VCR was downloaded from the Virginia Coast Reserve Long Term Ecological Research (VITA, 2011). The LiDAR-derived DEM with a cell resolution of 3.048 m, was created from LiDAR points (~1 m spacing) acquired in March 25–30, 2010. The horizontal and vertical datum are NAD83 and NAVD88, and the vertical accuracy was validated at less than 0.15 m. A water mask file was also attached to control for tidal regime during data collection. In our study, a coordinate transformation and a spatial resampling were first applied to the LiDAR-derived DEM to match the datum (WGS84 UTM 18N) and spatial resolution (30 m) of the Landsat images (Fig. 1d). Then, areas without tidal inundation were used to ascertain the elevation for each salt marsh vegetation community.

2.3.2. Field data and training samples

Field data is available for 17 sites marshes at the VCR from 1999 to 2014 (Christian and Blum, 2014). For each site, 4 transects were established for each marsh community (defined as creek bank, low marsh, high marsh, and transition). The location was determined with GPS and additional information, such as biomass, plant height, and population density, was also recorded. Only the sites of low marsh and high marsh were used to determine training samples of LM and HM, after extracting the annual invariant plots for them. The sites of creek bank and transition were not utilized. The zone of creek bank, which is just 5–10 m wide and usually adjacent to the lagoon or along tidal creeks, is not clear in Landsat images because of the coarse spatial resolution; the zone of transition, which also includes large quantities of shrubs, was grouped into the Scrub/Shrub class of NOAA C-CAP and thus screened out of our study.

By comparing the Landsat images with the classification map of McCaffrey and Dueser (1976) (Fig. S1), we obtained the texture and spectral characteristics of ULM and TF. These characteristics were

adopted to identify the invariant plots (training samples) of ULM and TF by overlaying several images from different decades and seasons. In total, 1391 pixels (including 331 for TF, 381 for LM, 365 for ULM, and 314 for HM) as training samples were employed from 40 invariant plots to build a classifier (Fig. 1b).

2.3.3. Water level data

Tidal level data were collected from NOAA Tides and Currents. The verified hourly water level data from the Wachapreague (no. 8631044) and the Kiptopeke (no. 8632200) tide gauge stations were used to determine the water level related to each Landsat image (Fig. 1a).

3. Methods

3.1. Assessment of available Landsat imagery

In coastal regions, frequent cloudy weather severely decreases the availability of satellite images and simultaneously reduces the reliability of classification results. Tidal flooding significantly affects vegetation reflectance, resulting in an underestimation of vegetation indices such as NDVI. Thus, an assessment of viable satellite imagery is the first step to guarantee high quality of time-series construction. We evaluated each image by cloud cover and tidal inundation using the NASA Landsat Ecosystem Disturbance Adaptive Processing System (LEDAPS) software, which provides a series of Landsat TM/ETM + products including surface reflectance, CFmask band (mask for clouds and cloud shadows), and LandWater band (distinguishing between land and water) (Zhu and Woodcock, 2012).

A two-step cloud cover filter strategy was proposed to avoid the cloud cover effect. First, a total of 379 Landsat images, including Landsat-4/5 TM during 1984–2011 and Landsat-7 ETM + scan off during 1999–2003 (Fig. 3a), were preliminarily filtered, eliminating all scenes with a cloud cover above 40%. Then, we further reduced the dataset to 254 scenes with a cloud cover percent less than 40%. The cloud cover percent was defined as:

$$\text{cloud cover percent} = \frac{A(\text{cloud}) + A(\text{cloud shadow})}{A(\text{salt marsh})} \times 100\% \quad (1)$$

Where, $A(\text{salt marsh})$ is the area of salt marsh. $A(\text{cloud})$ and $A(\text{cloud shadow})$ correspond to the area of clouds and cloud shadows falling on the salt marsh region. The clouds and cloud shadows for each image were detected by the CFmask band with the label values of 2 and 4.

To reduce the effect of different tidal stages, we determined a tidal height threshold above which the satellite image is less affected by tidal inundation. To ascertain this threshold, the tidal height for 254 candidate images was first calculated by the verified hourly water level data from the Wachapreague tide gauge station (no. 8631044), with linear interpolation to the time of image acquisition. This water level data covers the period during 1982–2005 and 2008–2011. The missing water data during 2006–2007 were indirectly approximated from the

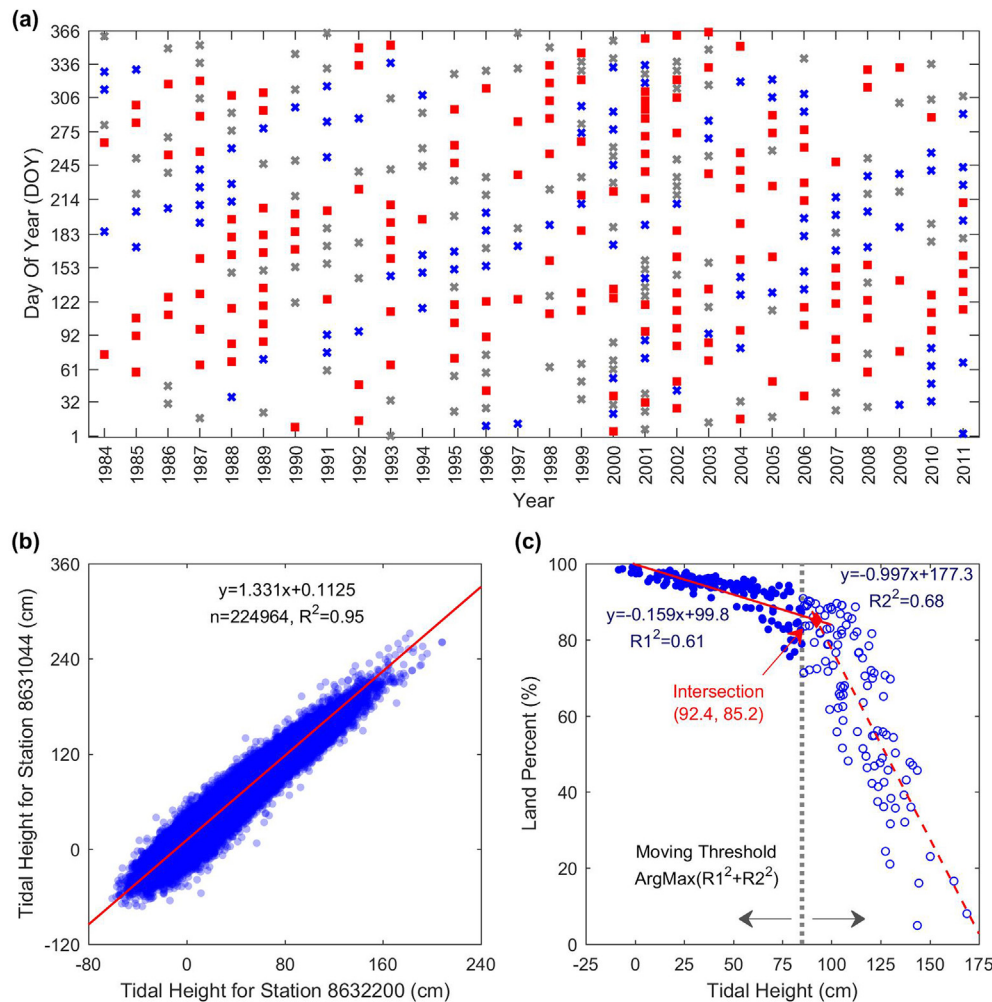


Fig. 3. Temporal distribution of all available Landsat TM/ETM + imagery during 1984–2011 filtered by cloud cover and tidal inundation. (a) Temporal distribution of 379 tiles of Landsat images. Gray crosses are 125 tiles eliminated due to cloud cover, blue crosses are 94 tiles eliminated due to tidal inundation, and red squares are the viable 160 tiles used for this study; (b) linear relationship between the tidal level data from Wachapreague (no. 8632200) and Kiptopeke (no. 8631044) stations during 1982–2005 and 2008–2011; (c) determination of inundation threshold by two discrete linear fits. (For interpretation of the references to color in this figure legend, the reader is referred to the Web version of this article.)

water data of the Kiptopeke station (no. 8632200) using a linear relationship (Fig. 3b).

For each tidal level, the merged part of land was separated from the submerged part using the LandWater band with the value of 0, thus determining the percent of land for each image. Results show that the percent of land first gradually decreases then rapidly drops for an increasing tidal level (Fig. 3c). The gradual decrease of exposed land mainly results from the submergence of tidal flats and salt marsh edges, which have a limited influence on our time-series classification and analysis of vegetation. The rapid drop of exposed land, on the other hand, is linked to the submergence of the marsh platform, compromising the analysis of salt marsh vegetation. Two discrete linear fittings are thus proposed to determine the critical tidal level threshold above which the marsh platform is flooded. The data were separated in two groups by a prescribed tidal level, and a linear fit applied to each group obtaining two coefficients of determination (R^2). By varying the tidal level from 0 to 150 cm with a step of 1 cm, the tidal height threshold was determined as the x-coordinate that maximizes the sum of the R^2 of the two linear fits. The purpose of maximizing the sum of the R^2 is to maximize the difference between the two groups of data and thus to delimit the boundary between gradual and rapid decrease of emergent land more precisely. The final threshold was 92.4 cm above MLLW. A total of 160 images had a water level below the threshold and were selected as viable images for our analysis (Table S1).

3.2. Construction of reference MNTS

Determination of the monthly sampling rate considered the tradeoff

between the revisit frequency of Landsat and the intra-annual phenological dynamics of salt marsh vegetation. During the period 1999–2003, more images are available from the two satellites (Landsat-5 TM and Landsat-7 ETM + SLC on) and allow the construction of a monthly Landsat time-series with a short time interval. 12 tiles of images acquired during 2001–2002 were selected and their detailed information referred in Table 1. These images were radiometrically corrected to surface reflectance using the LEDAPS software, which applies MODIS atmospheric correction to Landsat TM/ETM + data based on 6S radiative transfer model. The NDVI of each image was then calculated and combined in an orderly manner to build the reference MNTS.

Table 1
Detailed information of each image for the reference MNTS.

Acquisition Date (yyyy-mm-dd)	Satellite	Sensor	Cloud cover percent (%)	Land percent (%)	Tide height (cm)
2002-01-26	Landsat-5	TM	0.72	94.83	26.28
2002-02-19	Landsat-7	ETM +	4.86	75.57	78.81
2002-03-23	Landsat-7	ETM +	0.21	97.39	0.54
2001-04-29	Landsat-5	TM	4.71	92.04	68.50
2002-05-10	Landsat-7	ETM +	8.94	95.27	43.37
2002-06-11	Landsat-7	ETM +	19.47	88.30	78.58
2002-07-05	Landsat-5	TM	21.42	97.64	17.72
2001-08-27	Landsat-7	ETM +	0.06	95.78	34.83
2001-09-12	Landsat-7	ETM +	3.27	93.97	51.50
2002-10-01	Landsat-7	ETM +	5.97	94.85	35.43
2002-11-18	Landsat-7	ETM +	1.10	87.36	70.19
2001-12-25	Landsat-5	TM	10.02	94.34	46.22

3.3. C5.0 decision tree

The C5.0 algorithm was used to build classification decision trees in order to map salt marsh vegetation communities. This algorithm uses the information gain ratio criterion to determine the best attribute and possible threshold to separate different classes (Appendix a (Quinlan, 1999)). We adopted the C5.0 decision tree as the classifier due to its high classification accuracy and visible classification scheme. Supervised parametric classifiers such as Maximum Likelihood Classification (MLC) often deliver poor results when dealing with multi-modal data, because these classifiers assume a normal data distribution (Liu et al., 2011). Non-parametric supervised classifiers such as Classification And Regression Tree (CART), Support Vector Machine (SVM), and Artificial Neural Network (ANN) classifiers have no requirements regarding frequency distribution and have increasingly become popular for classifying remotely sensed data. However, the simple classifiers mentioned above may reach their limits in many applications due to the complex interplay between factors like scene complexity, scale, and aggregation (Marceau et al., 1994). In contrast, C5.0 decision tree introduces an ensemble classifier method—boosting, which works by repeatedly running the C5.0 algorithm on various distributions over the training samples, and then combines multiple classifiers into a single composite classifier (Appendix b, see (Quinlan, 1996)). By this means, the boosting ensemble C5.0 decision tree could avoid some errors from the single classifiers it contained and is more stable and robust to noise in the training samples (DeFries and Chan, 2000; Miao et al., 2012). Compared to the Random Forest (RF) classifier, which also ensembles the boosting algorithm, the C5.0 usually yields similar classification accuracies but allows for the view of the established rules with regard to the impact of individual features (Waske and Braun, 2009), making it widely applicable in the field of remote sensing (de Colstoun and Walther, 2006; Esch et al., 2014; Sun et al., 2016).

In our study, the 1391 pixels of training samples were used to build the C5.0 decision tree, whose accuracy was verified by the 1000 points of testing samples. To set the parameters of the decision tree, NDVI from different months served as attributes and the confidence level and minimum case were set to 0.25 and 15 (almost 1% of training data), respectively. Ten decision trees were built by the boosting algorithm.

3.4. Construction of flexible MNTS

Note that the MNTS strategy is hard to be directly applied to all viable Landsat images due to their irregular and scattered temporal distribution (Fig. 3a). For example, since 1984, the earliest viable image from December appeared in 1992. Therefore, if we directly use the MNTS method, which requires the NDVI from each month, the classification map will span 9 years (from 1984 to 1992). The accuracy of this map would be low since vegetation likely changed during such a long time interval. To circumvent the lack of suitable Landsat imagery in some years, we used the NDVI of only few key months rather than the values of 12 months. A two-step procedure including reference subset assessment and iterative selection was proposed to construct the flexible MNTS (Fig. 4). The whole procedure was automatically implemented in Matlab and R software.

Reference subsets assessment. In order to determine the optimal MNTS, the overall accuracy of each possible subset (i.e., NDVs from a combination of a different number of months, from 1 to 12) from the reference MNTS (hereafter referred as the predicted accuracy) was assessed (Fig. 4a). Such predicted accuracy does not take into account all the aspects of classification, but it is intuitive and proven to give results similar to more complex indexes for each subset. For a 12-month time-series dataset, the total number of subsets is calculated by:

$$\sum_{i=1}^{12} C(12, i) = C(12,1) + C(12,2) + \dots + C(12,12) = 2^{12} - 1 \quad (2)$$

Where, $C(12, i) = \frac{12!}{i!(12-i)!}$ denotes the number of possible subsets of i months from a set of 12 months. In our study, a total of 4095 different subsets of MNTS were tested (Fig. 4b). We can thus build a look-up table with the accuracy of all subsets of images with different number and combination of months. The accuracy is only computed for the 2001–2002 period, but it can be used to approximate the accuracy of any other subset of images taken from that combination of months. Although time consuming, this exhaustive process enables to compare the classification efficiency among all subsets, which would not be possible in common variable selection processes.

Iterative selection. After the predicted accuracies were assigned to all subsets, the total number of classification maps as well as the average time interval between classification maps for the period 1984–2011 can be calculated for a given predicted accuracy with an iterative process (Fig. 4c). We first create an empty collection to store image information (i.e., acquisition date, cloud cover percent, and tide height). Then, we read the information of the next viable image: if the month of the image does not appear in the collection, we add the information of the image to the collection; if the month of the current image is already present in the collection, we choose the image with lowest tidal height and cloud cover percent, discarding the other one. In this way, a series of subsets with a different number of images are created. The subsets span time intervals of different length with a different combination of months. For each subset, we determine the predicted accuracy by referring to the accuracy of the reference subset having the same set of months. For example, if the subset contains images from February, March, and September, we assign to it the overall accuracy of the 2001–2002 subset with images from February, March, and September. If the predicted accuracy of the subset is greater than the target one, the subset is chosen, and its information (e.g., combination of images, time interval) is stored for subsequent classification map. Afterwards, the collection is reset to prepare for the next flexible MNTS. The above process is repeated starting from the next viable image until all images are used. Finally, the average time interval between two classification maps is computed as the ratio between 28 (the number of years between 1984 and 2011) and the number of generated maps. With this method a series of multi-temporal classification maps of salt marsh vegetation communities is generated based on the information from the whole flexible MNTS.

4. Results

4.1. Comparison between MNTS and multi-spectral images

The Surface Reflectance curves of Multi-Spectral image (SRMS) and the MNTS curves are presented in Fig. 5 for four vegetation classes (TF, LM, ULM, and HM). For the MNTS curves, temporal NDVI differences can discriminate all types of marsh communities (Fig. 5a). TF is characterized by very low NDVI values in all seasons, especially between July and October, which is the optimal period for its identification. Although the NDVI curves for the three salt marsh communities have a similar trend—the NDVI peaks during the late growing season (August to September) while the minimum is in late winter (February to March)—differences are still present among them. The NDVI of LM is usually lower in almost every month, facilitating the discrimination of this community; the NDVI of HM is higher in summer (from June to August), indicating HM may be easily identified during this period. For the curves of SRMS, the differences of the four classes are mainly present in Band 4 (Near Infrared: 0.76–0.90 μm), Band 5 (Shortwave Infrared 1: 1.55–1.75 μm), and Band 7 (Shortwave Infrared 2: 2.08–2.35 μm), and the differences reach a maximum between June and September (Fig. 5b–m). However, even during this period, the discrimination of each class is not perfect: HM can be easily identified, but for the other salt marsh communities (TF, LM, and ULM), the low differences and the high standard deviations prevent discrimination.

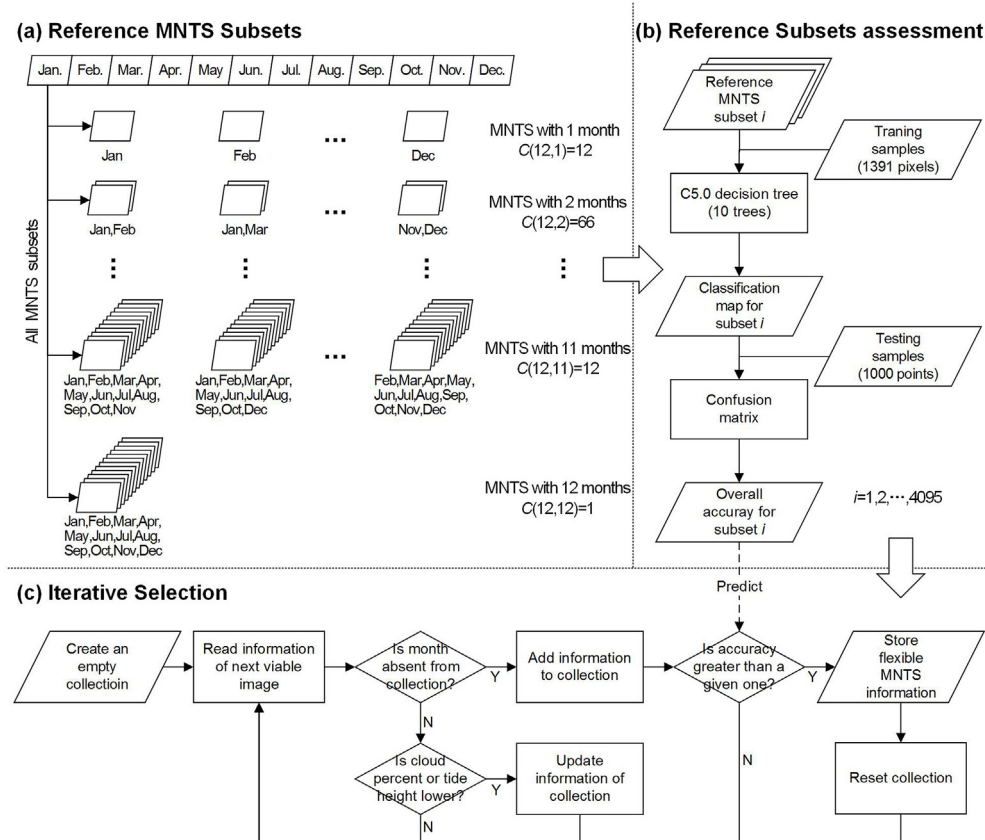


Fig. 4. Flow diagram depicting the method of flexible MNTS. The whole process include (a) construction of the reference MNTS subsets, (b) reference subsets assessment, and (c) iterative selection for a given accuracy.

The accuracy of the classification maps derived from MNTS and SRMS was calculated with the confusion matrix method (Foody, 2002b), based on 1000 points of testing samples derived from the NAIP 2004 aerial photograph. MNTS accuracy is higher than the accuracy of multi-spectral images (Fig. 6). Specifically, the overall accuracy using one multi-spectral image is on average 0.791; it reaches a peak of 0.823 in July and a minimum of 0.747 in January (Fig. 6a). The user's and producer's accuracies for each class are variable and usually display low values: the user's accuracies for TF in winter (December to February) are always lower than 0.400 and the producer's accuracy for ULM in January is merely 0.634 (Fig. 6b and c). In contrast, the overall accuracy of the classification map using MNTS reaches 0.898, approximately 0.107 higher than the average accuracy of multi-spectral images. Except for TF, the user's and producer's accuracies for each class are always above 0.840, yielding to a good classification result. The most striking improvement using MNTS is attained on the user's accuracy of TF, which increases from 0.553 (multi-spectral image in June) to 0.729. The producer's accuracy of ULM reaches 0.901 with MNTS, exceeding by 0.087 the highest producer's accuracy of multi-spectral images. These results are in agreement with what we have found in the spectral analysis.

4.2. Relationship between predicted accuracy and average time interval between classifications

Predicted accuracy varied as a function of the number of months and month subsets used for classification mapping (Fig. 7a). In general, the average predicted accuracy rises with the number of months used in the analysis, while the variability in accuracy among subsets having the same number of months decreases. For subsets using a high number of months in the time-series construction, the increment in accuracy is not

very large, indicating that an excessive number of months could be inefficient for the purpose of accuracy improvement. For example, the maximum predicted accuracy (0.898) is reached using images from only 10 months (Fig. 7a and b). February and August are relatively important for the identification of salt marsh vegetation communities, since 28 (82.3%) of the 34 subsets with the highest accuracies include the NDVI of these months (Fig. 7b).

Using a large number of months in the analysis increases the time interval between classification maps, affecting the temporal resolution of the study. To determine the optimal subset, we plot the average time interval between two subsequent maps as well as the number of resulting maps as a function of predicted accuracy (Fig. 8). The predicted accuracy linearly decreases with the number of maps ($R^2 = 0.98$). A total of 26 classification maps can be obtained for a predicted accuracy of 0.78. In turn, the number of maps sharply decreases to 4 for a predicted accuracy of 0.89. The average time interval between maps increases from 1 year for an accuracy of 0.78–7 years for an accuracy of 0.89 with an inverse hyperbolic relationship ($R^2 = 0.96$). In general, the higher is the chosen accuracy, the lower the number of maps and the longer the average time interval between maps are, reducing the effectiveness of the analysis. Based on these results, we choose 8 classification maps separated on average by 3.5 years with a predicted accuracy of 0.86 (Table 2).

To further validate our method, the classification map of 1988 was compared with the map of McCaffrey and Dueser (1976), yielding an accuracy of 0.778. Four classification maps acquired after 2000 were also verified with labeled random validated points based on each NAIP image. It is worth noting that the average overall accuracy for the classification maps was 0.844, lower than the predicted value (Table 2). This discrepancy between predicted and validated accuracy is probably due to changes in image quality for time-series construction and the

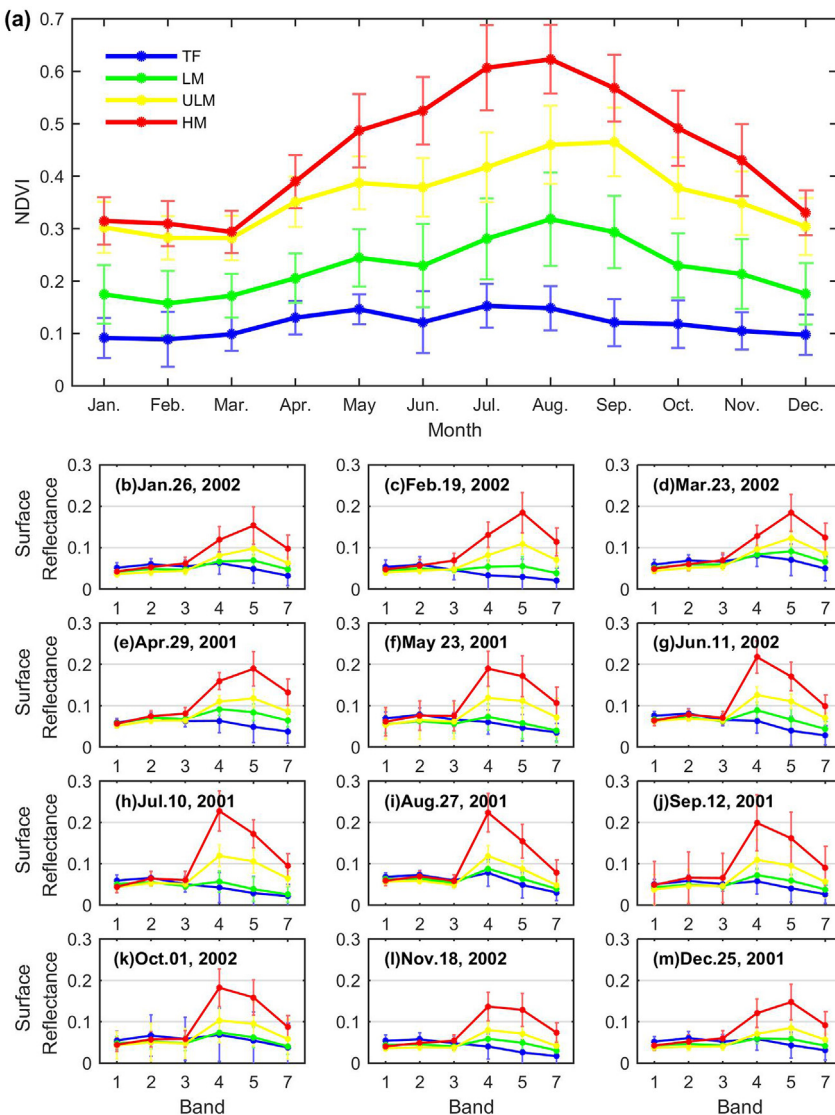


Fig. 5. Monthly NDVI Time-Series (MNTS) and Surface Reflectance of Multi-Spectral image (SRMS) for four classes (TF: tidal flat, LM: low marsh, ULM: upper low marsh, and HM: high marsh). (a) MNTS curves for the four classes; (b)–(m) multi-spectral surface reflectance curves for the four classes in different months. Node represents the mean value and error bar represents the standard deviation.

long time interval between classification maps (details in section 5.2).

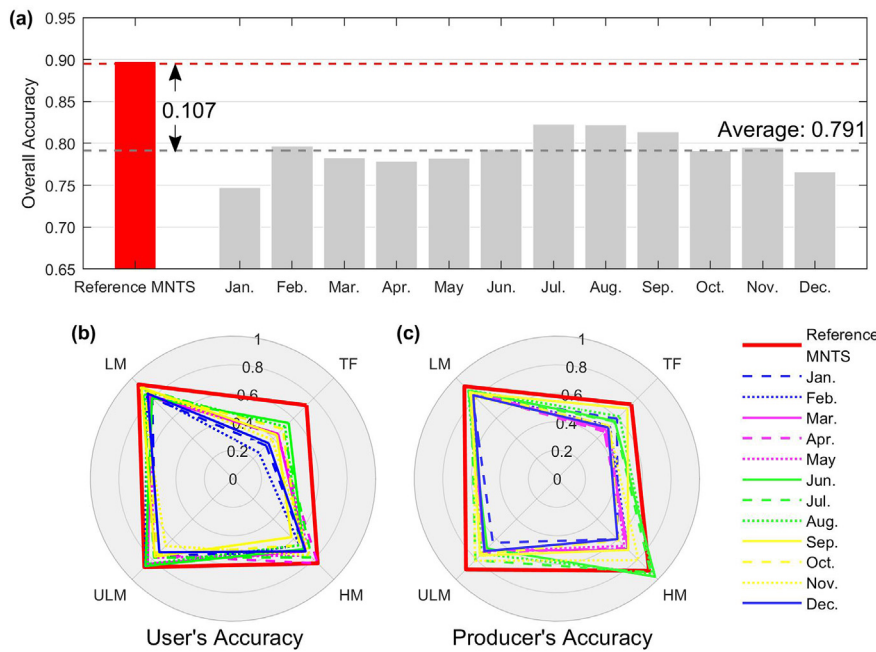
4.3. Elevation of salt marsh vegetation communities

The LiDAR-derived DEM of 2010 and the classification map of 2011 were compared to extract the elevation for each class at a pixel level. The elevation distributions for each class are shown in Fig. 9. TF displays a large distribution of elevations because un-vegetated overwash fans and salt flats having high elevation are included in this class. Differences in elevation among classes are significant (one-way ANOVA -ANalysis Of Variance-with unequal sample sizes, TF: 11752, LM: 88399, ULM: 43361, HM: 6712, (Tamhane, 1977)). The Mean Square of elevation between classes (MS_b , 2570.34) is much larger than the Mean Square of elevation within classes (MS_w , 0.17). As a ratio between MS_b and MS_w , the F statistic equals to 15458.14, which is extremely high and renders the p-value less than 0.05. That indicates the average elevation of the four classes is not the same at the confident level over 95%. The one-way ANOVA indicates whether the results are significantly different in general, but it does not specify what classes are different. The Tukey HSD (Honestly Significant Difference) can be used in conjunction with the ANOVA to find what pairs of classes have a

mean elevation significantly different (Tukey, 1949).

From all 6 pairwise comparisons, both lower and upper confidence intervals are uniformly negative even for neighboring classes (i.e., TF-LM, LM-ULM, and ULM-HM); therefore the average elevation of any class is significantly different from the others (Table 3). Quantitatively, with the confidence level over 95%, the elevation of TF is 0.525–0.546 m lower than the elevation of LM, the elevation of LM is 0.268–0.281 m lower than the elevation of ULM, and the elevation of ULM is 0.200–0.227 m lower than the elevation of HM. Salt marsh vegetation communities are therefore segregated by elevation, and might respond to sea level rise and vertical sediment deposition (details in section 5.4).

As it is common in salt marshes, the elevation distributions between adjacent marsh communities partly overlap. This is because many factors control vegetation zonation, including hydroperiod, distance from the nearest creek, salinity, and edaphic conditions (Silvestri et al., 2005). In particular, elevation is only a coarse approximation for hydroperiod. It is also worthy to note that LiDAR-derived DEM in salt marshes are prone to errors because the low and even vegetation canopy has been found to limit laser pulse penetration, resulting in an overestimation of marsh ground elevations (Marani et al., 2006; Rosso et al., 2006). Despite these limits, we find that the elevations of



different salt marsh communities are statistically different (one-way ANOVA and Tukey HSD).

4.4. Spatial and temporal variations in salt marsh vegetation communities

The classification map of 2011 (Fig. 10) indicates that TF, LM, ULM,

and HM account for 11.3% (36.4 km^2), 62.7% (201.4 km^2), 20.1% (64.4 km^2), and 5.9% (19.0 km^2) of the VCR area, respectively. North of Cedar Island ULM and HM are more common, whereas LM dominates the bays south of Cedar Island (Fig. 10a–c). Unvegetated TF areas comprise washover deposits, small tidal creeks, and eroded marsh area (Fig. 10c–g). Note that here we only consider areas within the NOAA C-

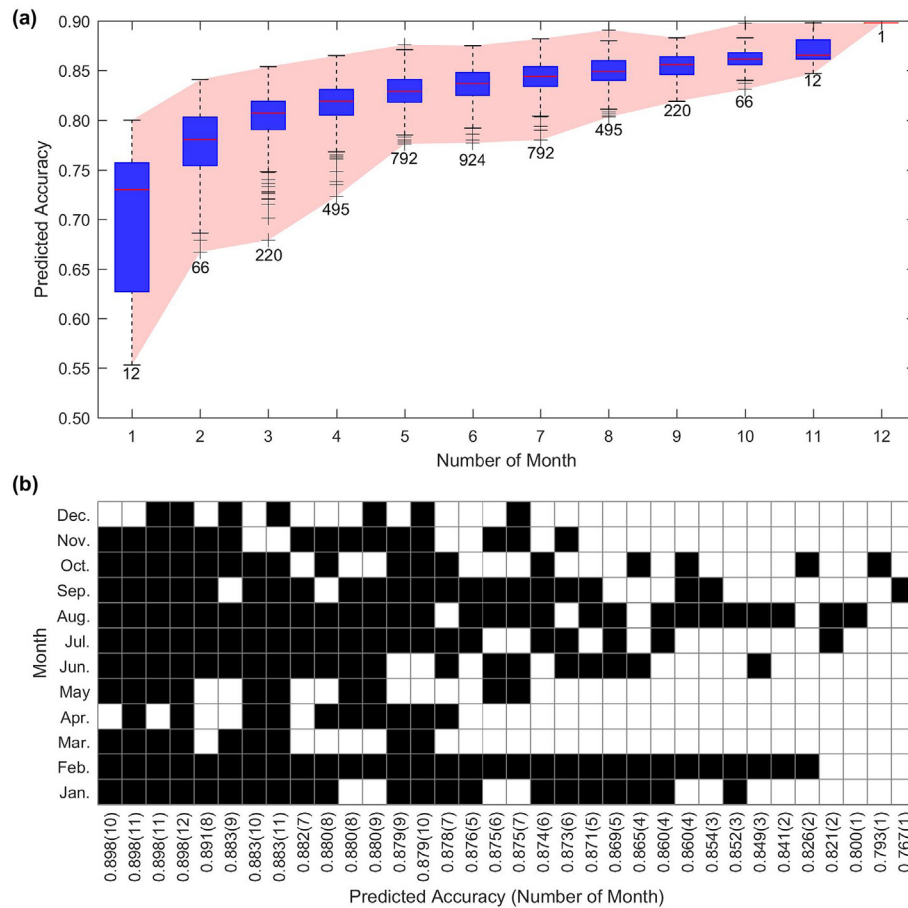
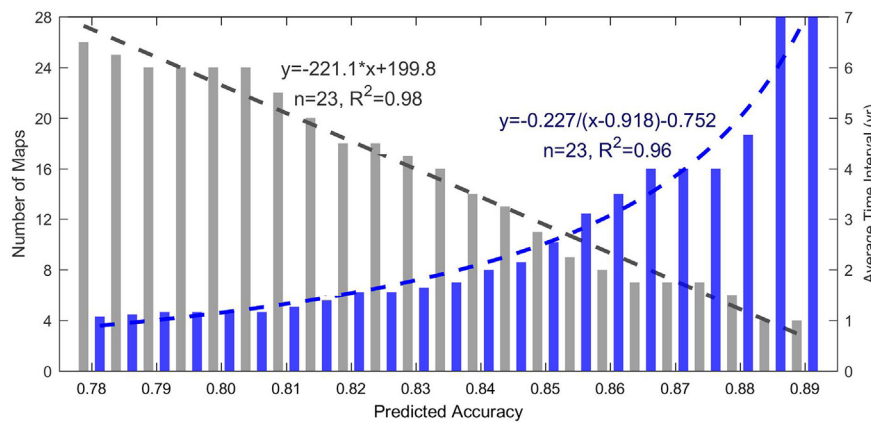


Fig. 7. (a) Predicted accuracy as a function of the number of months used in the MNTS. Labeled values represent the total number of subsets considered using that number of months. The horizontal red line in the box is the median value, the lower and upper horizontal lines denote the first (Q1) and the third quartile (Q3), the interquartile range (IQR) equals to Q3–Q1. The horizontal line above (below) the box is the greatest (least) value within Q3+1.5 IQR (Q1–1.5 IQR), values higher than 1.5 IQR are represented as crosses. The red envelop indicates the extent between the minimum and the maximum accuracy values; (b) subsets having the three highest accuracies for a given number of months used in the analysis (black squares mean that a particular month was selected for that subset, in parenthesis the number of months). (For interpretation of the references to color in this figure legend, the reader is referred to the Web version of this article.)



CAP class of Estuarine Emergent Marsh, therefore TF represent areas that used to be vegetated at the time of the NOAA classification and eventually became un-vegetated because of different processes.

By comparing the 8 classification maps (Fig. 10, Fig. S2–S8), TF and HM experienced a significant increase in area from 1984 to 2011 (15.1 and 5.0 km² respectively), accompanied by a large reduction in ULM (15.5 km²) and a subtle decrease in LM (4.6 km²) (Fig. 11a). A significant quadratic polynomial relationship can be fitted between year and the cumulative percent of area change (Fig. 11b). The diverse curvatures of the fitting curves suggest two different evolution trajectories: one for TF and HM, whose increment in area mainly took place before 2000, the other for ULM, whose area decreased after 2000. Between 1988 and 2011, only a small part of the area underwent vegetation conversion, and 93.6% of the change involved neighboring salt marsh vegetation communities (i.e., TF to LM, LM to ULM, and ULM to HM, Fig. 11c). The conversion from LM to TF and from ULM to LM and HM are the most sizable. 20.1 km² of LM has been replaced by TF,

either through erosion of marsh boundaries in the southern part of the VCR or through overwash events that buried marsh vegetation in the backbarrier area. 6.4 km² of ULM became HM, mostly in the marshes between Cedar island and the mainland; 13.8 km² of ULM scattered in the whole area were transformed in LM.

5. Discussion

5.1. Classification uncertainty from MNTS

Unlike classification maps from single images, the accuracy of which is based on the ability to discriminate spectral characteristics, the classification based on MNTS relies on the temporal stability of each class during the time interval selected for the classification (Feilhauer et al., 2013). On the premise of high separability for each class, the accuracy will be high if the classes are stable, otherwise the accuracy will be low. From this point of view, clouds and cloud shadows, tidal

Table 2

Detailed information of 8 classification maps obtained in the period 1984–2011 with the flexible MNTS approach.

Classification Map	Period/Time interval (yr)	Information for flexible MNTS (Date_Satellite_Sensor)	Reference Map	Validated Accuracy
1988	1984–1988/5	1985-02-28_Landsat-5_TM 1987-03-06_Landsat-5_TM 1987-05-09_Landsat-5_TM 1988-07-14_Landsat-5_TM 1984-09-21_Landsat-5_TM 1987-10-16_Landsat-5_TM 1987-11-17_Landsat-5_TM	McCaffrey and Dueser (1976)	0.778
1992	1989–1992/4	1992-01-15_Landsat-5_TM 1989-03-27_Landsat-5_TM 1989-04-12_Landsat-5_TM 1989-06-15_Landsat-5_TM 1989-07-25_Landsat-4_TM 1989-10-21_Landsat-5_TM 1989-11-06_Landsat-5_TM	–	–
1996	1993–1996/4	1996-02-11_Landsat-5_TM 1995-03-12_Landsat-5_TM 1993-07-12_Landsat-5_TM 1995-09-04_Landsat-5_TM 1995-10-22_Landsat-5_TM 1996-11-09_Landsat-5_TM 1993-12-19_Landsat-5_TM	–	–
1999	1997–1999/3	1998-04-21_Landsat-5_TM 1999-07-05_Landsat-7_ETM + 1999-08-06_Landsat-7_ETM + 1999-09-23_Landsat-7_ETM + 1998-10-30_Landsat-5_TM 1999-11-18_Landsat-5_TM 1998-12-01_Landsat-5_TM	–	–
2002	2000–2002/3	2002-01-26_Landsat-5_TM 2002-02-19_Landsat-7_ETM + 2002-03-23_Landsat-7_ETM + 2000-05-04_Landsat-7_ETM + 2002-06-11_Landsat-7_ETM + 2001-08-03_Landsat-5_TM 2001-09-12_Landsat-7_ETM + 2001-10-22_Landsat-5_TM 2002-11-18_Landsat-7_ETM +	NAIP 2004	0.869
2005	2003–2005/3	2005-02-19_Landsat-5_TM 2003-03-10_Landsat-7_ETM + 2004-04-05_Landsat-5_TM 2005-06-11_Landsat-5_TM 2004-08-11_Landsat-5_TM 2005-10-01_Landsat-5_TM 2003-11-29_Landsat-5_TM	NAIP 2005	0.838
2007	2006–2007/2	2006-02-06_Landsat-5_TM 2006-04-11_Landsat-5_TM 2007-05-16_Landsat-5_TM 2006-08-01_Landsat-5_TM 2006-09-18_Landsat-5_TM 2006-10-04_Landsat-5_TM	NAIP 2008	0.848
2011	2008–2011/4	2008-02-28_Landsat-5_TM 2009-03-18_Landsat-5_TM 2009-05-21_Landsat-5_TM 2008-06-03_Landsat-5_TM 2011-07-30_Landsat-5_TM 2010-10-15_Landsat-5_TM 2008-11-10_Landsat-5_TM	NAIP 2011	0.821

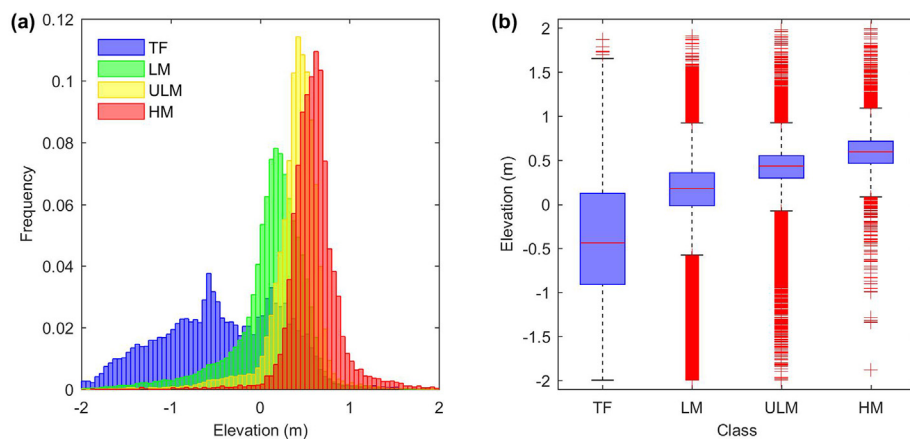


Fig. 9. LiDAR-derived elevation distributions for the four classes (TF, LM, ULM, and HM) depicted by (a) histogram plot and (b) box plot. (The horizontal red line in the box is the median value, the lower and upper horizontal lines denote the first (Q1) and the third quartile (Q3), the interquartile range (IQR) equals to Q3–Q1. The horizontal line above (below) the box is the greatest (least) value within Q3+1.5 IQR (Q1–1.5 IQR), values higher than 1.5 IQR are represented as crosses. (For interpretation of the references to color in this figure legend, the reader is referred to the Web version of this article.)

Table 3
Pairwise comparison results based on Turkey HSD post-hoc analysis.

Class 1	Class 2	Lower confidence interval	Estimate	Upper confidence interval	p value
TF	LM	-0.546	-0.537	-0.525	5.96E-08
TF	ULM	-0.821	-0.810	-0.799	5.96E-08
TF	HM	-1.040	-1.024	-1.008	5.96E-08
LM	ULM	-0.281	-0.274	-0.268	5.96E-08
LM	HM	-0.501	-0.488	-0.475	5.96E-08
ULM	HM	-0.227	-0.214	-0.200	5.96E-08

oscillations, and a sudden conversion from one vegetation community to another can give rise to uncertainties in the MNTS classification.

A 40% threshold for the clouds filter still allows some clouds and cloud shadows in the images, possibly reducing mapping accuracy (Fig. 12b). Notwithstanding, only in few cases a region was covered by clouds for more than one image of the time series, so that information from consecutive images was able to fill the gap through the boosting algorithm of the C5.0 decision tree (Appendix b). As an example, the region with yellow dash circles affected by cloud cover in July 2002 (Fig. 12b) was still discriminated by MNTS in the classification maps (Fig. 12f). Tidal creeks and adjacent ponding areas present another challenge for time-series classification because they are subject to flooding at high tide. When the tidal level is low, these regions are identified as LM, because of the marsh vegetation bordering the creeks (Fig. 12a); when the tidal level is high, the regions are likely classified as TF, since the sparse vegetation is mostly submerged, leading to NDVI values closer to open water or mud flat (Fig. 12e). Voted by each tree from the boosting algorithm, the final classification map presents a comprehensive result, which is only partly affected by any individual image of the time series (Fig. 12f).

The accuracy of the TF class in these regions is relative low (Fig. 6b and c). Because the testing samples of TF were generated from random points, some of them fell in ponding areas and near retreating or prograding marshes, where the conversion from TF to salt marsh or vice versa is fast. On the other hand, the training samples of TF, which were used for classification mapping during different periods, were selected within relatively stable tidal flats. As a result the accuracy for TF is quite unsatisfactory even when MNTS are used, which seems in contradiction with the observed high separability (Fig. 5a).

5.2. Discrepancy between predicted and validated accuracy

To further explore the difference between predicted and validated accuracy, we generated the classification maps during 2004–2011 at different predicted accuracy levels. Their overall accuracy was subsequently validated using testing samples from each NAIP image. The average validated accuracy is less than the predicted accuracy

(Fig. 13a), and the difference between predicted and validated accuracy is higher when the predicted accuracy is either small (< 0.79) or large (> 0.86).

The classification maps produced with a low predicted accuracy include single NDVI classifications, resulting in a low validated accuracy. This is because single NDVI classification is heavily affected by clouds and shadows, since the missing information in the clouds area cannot be replaced by other images. For a high predicted accuracy, more months are integrated in the time series and the time interval between each classification map is long. For example, when the predicted accuracy is over 0.86, only two classification maps can be acquired for the period 2004–2011, each spanning at least 4 years. During such long periods, changes in vegetation communities at the ecotones cannot be ignored, leading to a difference between classification maps and NAIP images. Consequently, the difference between predicted and validated accuracy becomes larger, despite the increase in predicted accuracy (Fig. 13a). In contrast, all images from the reference MNTS were acquired in only two years (2001–2002), reducing the error due to vegetation change. This effect is also the cause of the low accuracy (0.778) obtained by comparing the classification map of 1988 and that of McCaffrey and Dueser (1976), taken 13 years apart. For a predicted accuracy between 0.79 and 0.86, the difference between the predicted and validated accuracies is quite small, and it is likely due to the quality of the images: the images from the flexible MNTS of 2002 have fewer clouds and lower tidal levels (Fig. 13b and c). The correlation between predicted and validated accuracy can be well represented ($R^2 = 0.96$) by a linear function, which differs of merely 0.0194 from the standard 1:1 line (Fig. 13a). We can thus trade off high accuracy for a short time interval between classification maps, as long as we avoid either small predicted accuracies affected by image quality or large predicted accuracies affected by changes in vegetated surfaces.

The advantages of the flexible MNTS increase when two or more remote sensors are used (e.g. TM and ETM+, Fig. 3a). With more satellites entering in operation with spectral distribution and spatial resolution similar to Landsat TM/ETM+ (e.g., Landsat-8 OLI, Sentinel-2 MSI, HJ-1 CCD), the increased availability of images for time-series construction will reduce the difference between predicted and validated accuracy, paving the way to a more robust application of our method.

5.3. Detection of vegetation shift at the edges of marsh patches using MNTS

Changes in vegetation cover are high near the edge of marsh communities. Because most of the testing samples do not fall near the edge, the classification errors in these areas may not be well described by the overall accuracy. Therefore, it is necessary to determine how MNTS detect shift at the edge of marsh patches. We overlap classification maps spanning the period 1984–2011 by chronological order (Fig. 14a) and define salt marsh behavior pixel by pixel as follows. If the class of a

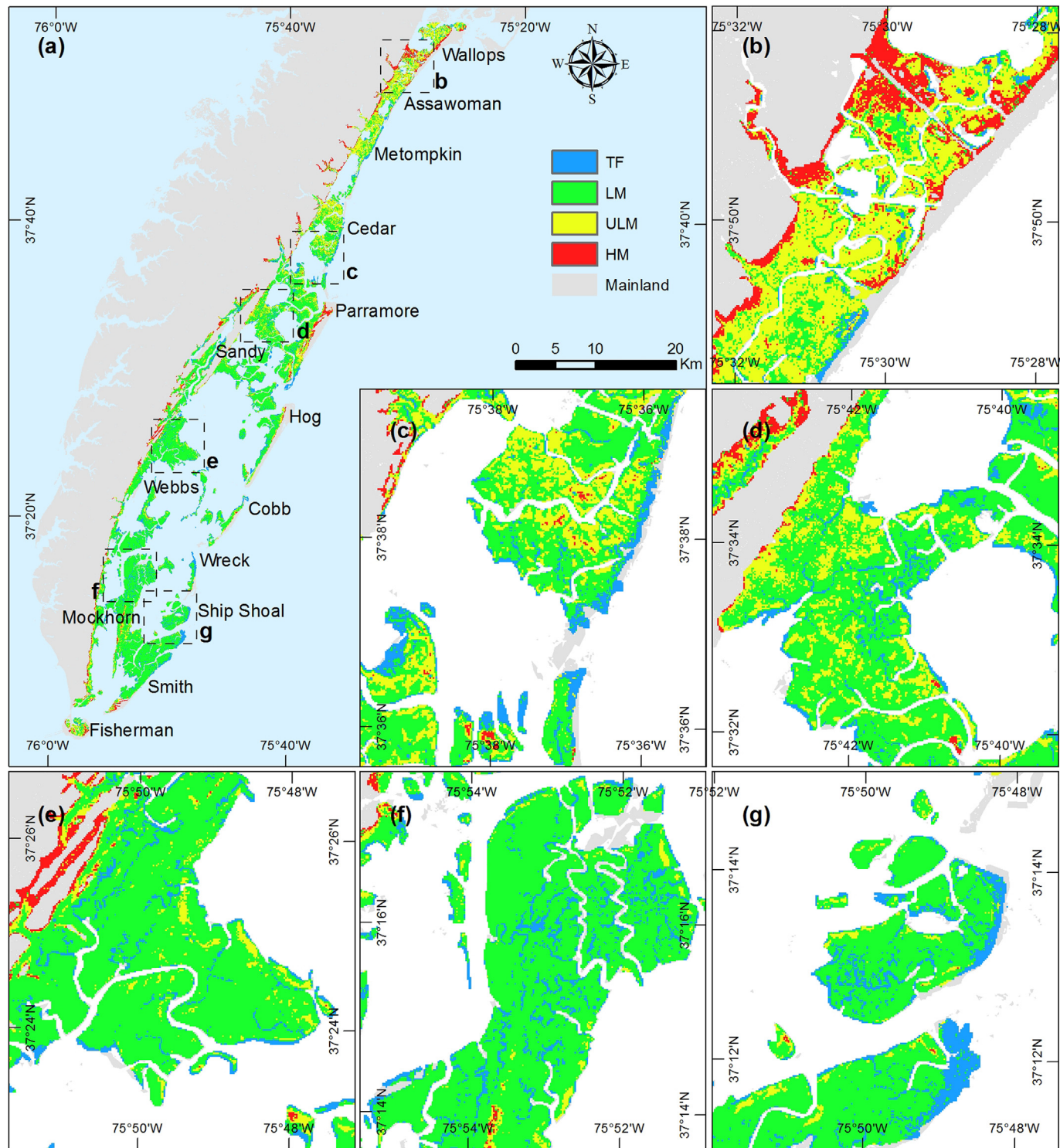


Fig. 10. Classification maps of salt marsh vegetation communities in 2011 based on the reference MNTS. (a) Overview classification map of the entire VCR, (b)–(g) detailed classification maps of six sites within the VCR.

pixel remains unchanged in all classification maps, the pixel is defined as stable (Fig. 14b stable line). The regions constituted by stable pixels are the innermost areas of a vegetation community. The remaining pixels, whose class changed between 1984 and 2011, were regarded as the edge of marsh patches. Since the evolution of coastal salt marsh communities is usually directional, and often linked to a relative elevation change (Isacch et al., 2006; Lenssen et al., 1999), the marsh edge can be further be divided into two subtypes: if the class of a pixel has

experienced change with a consistent direction (e.g. the class converted from HM to ULM and further to LM), the pixel would be grouped into the shifting group (Fig. 14b shifting line 1–3); if the class of a pixel experienced changes with divergent directions (e.g., the class converted from TF to LM and then converted back to TF), we add the pixel into the oscillating group (Fig. 14b oscillating line 1 and 2). Further, we assess the ability to detect vegetation change at three sites: shifting pixels were selected from site 1 (characterized by ULM and HM Fig. 14d) and

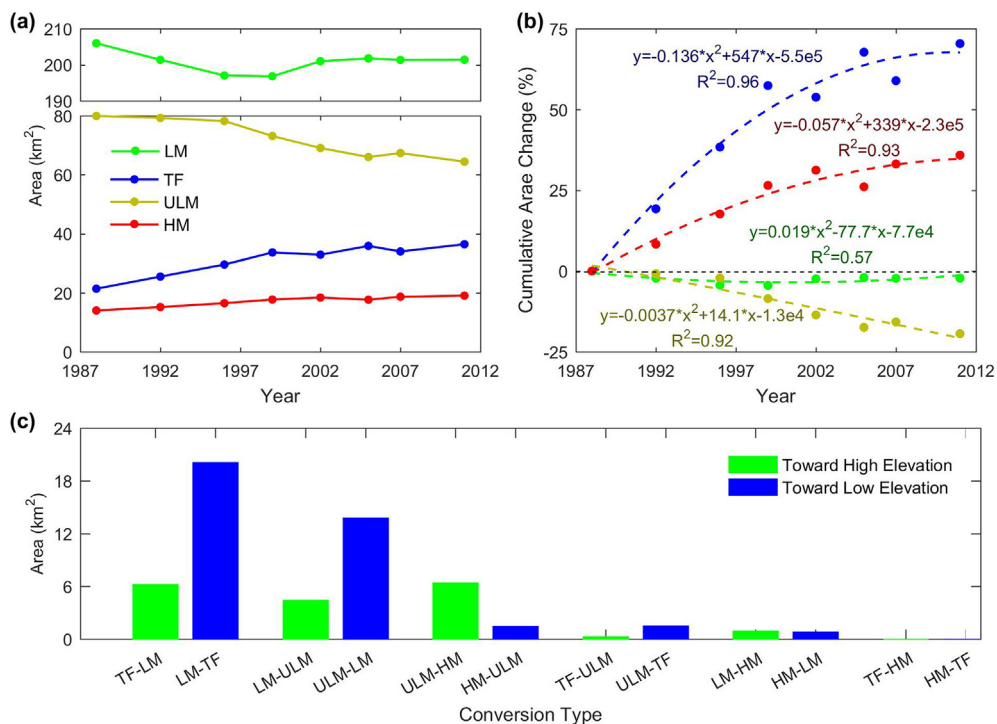


Fig. 11. (a) Total area change for each vegetation community determined by 8 classification maps. (b) Percent of area change for each salt marsh vegetation community; (c) conversion area for each pair of salt marsh vegetation communities in the period 1984–2011.

site 3 (characterized by TF and LM, Fig. 14f), and oscillating pixels were selected from site 2 (characterized by LM and ULM, Fig. 14e).

The MNTS strategy we propose determines the vegetation shift of the marsh edge based on long-term NDVI variations. A total of 160 viable Landsat images were used to construct long-term NDVI series,

whose variability was fitted by a modified sine function (Fig. 15):

$$y = (ax + b)\sin(x/w + t) + p_1 x + p_2 \quad (3)$$

Where x denotes number of days, y denotes average NDVI, $x/w + t$ denotes phase, $ax + b$ and $p_1 x + p_2$ denote amplitude and offset,

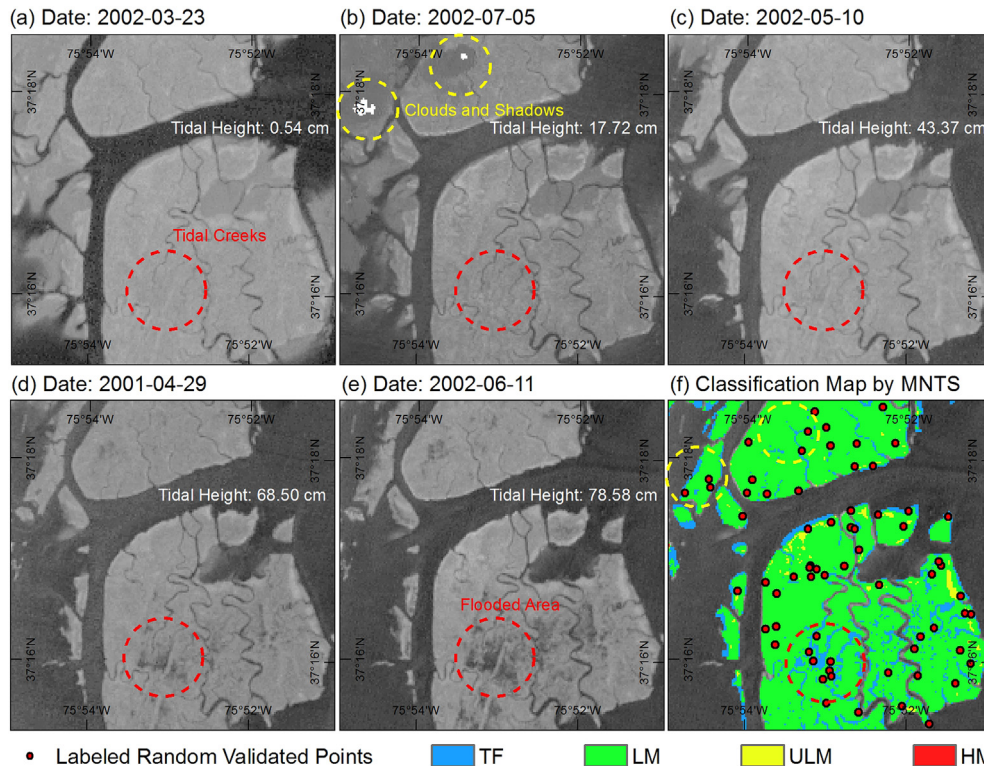


Fig. 12. MNTS classification uncertainty due to cloud cover and tidal inundation. (a)–(e) NDVI images acquired at different tidal levels; (f) final classification map for salt marsh vegetation communities and distribution of labeled random validated points based on the NAIP image of 2004.

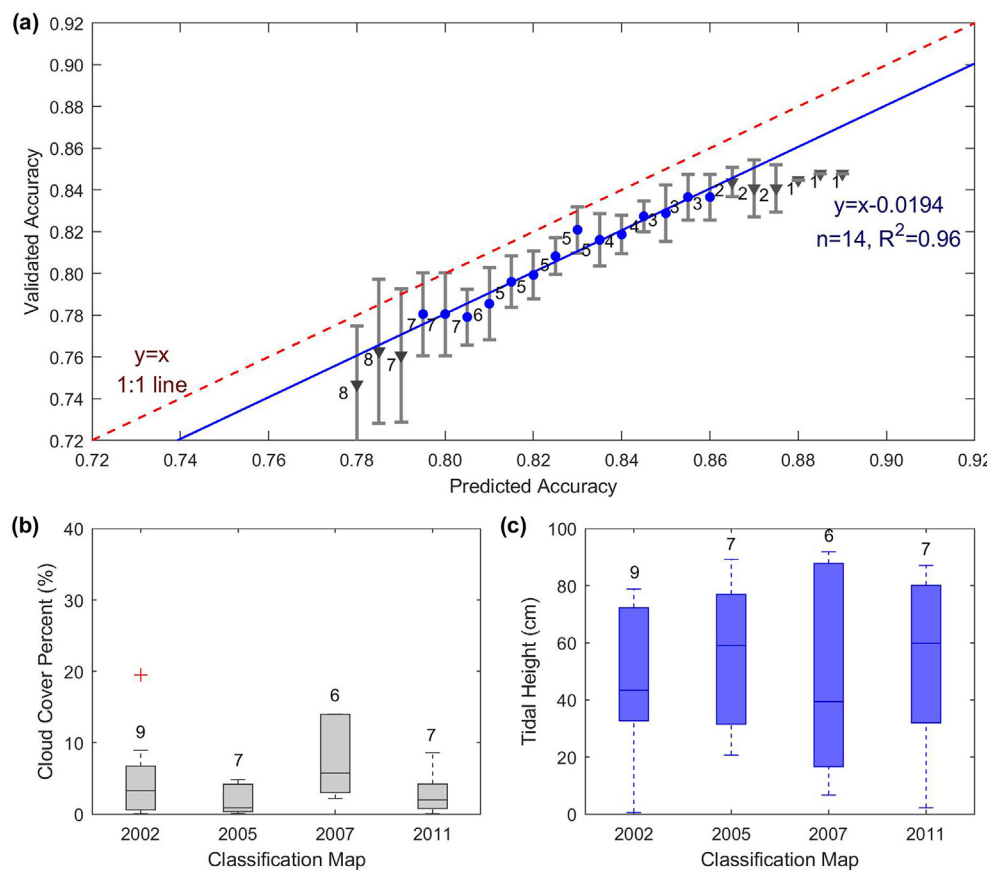


Fig. 13. Difference between predicted and validated accuracy and related causes. (a) Relationship between predicted accuracy and validated accuracy (nodes represent the mean values and error bars represent the standard deviation for the validated accuracy, number of classification maps is indicated); (b) and (c) distributions of cloud cover percent and tidal levels for the images used in each classification map (The horizontal red line in the box means the median value, the lower and upper horizontal line denote the first (Q1) and the third quartile (Q3), the interquartile range (IQR) equals to Q3-Q1. The horizontal line above (below) the box is the greatest (least) value within Q3 + 1.5 IQR (Q1-1.5 IQR), values more than 1.5 IQR are represented as crosses. The number of images used in the flexible MNTS construction is indicated). (For interpretation of the references to color in this figure legend, the reader is referred to the Web version of this article.)

respectively.

This fitting function assumes that NDVI variations are periodical with a possible long-term trend. For the shifting pixels of site 1, the NDVI fitting curve is very similar to that of ULM at the beginning of the time interval (Fig. 15a), in time it becomes closer to HM, with a higher offset and amplitude (Table S2). The shift from ULM to HM is so evident that MNTS can easily capture the whole process. The shifting pixels of site 3 display a similar behavior. Here a large increase in NDVI translates in a sharp increment of both offset and amplitude of the fitting curve (Table S2), and support the shift from TF to LM in the period 1984–2011 (Fig. 15c). In the oscillating pixels of site 2, the NDVI fitting curve is neither similar to LM nor ULM between 1984 and 1992 (Fig. 15b). As a result it is difficult to determine whether the NDVI variations are related to a shift in vegetation community. Therefore, MNTS are able to detect vegetation shifts having a consistent direction (i.e., shifting pixels) but fail to determine the vegetation evolution in pixels experiencing shifts with divergent directions (i.e., oscillating pixels). In general, 87% salt marshes in the VCR are likely to be accurately classified by the MNTS strategy, including 75.2% pixels in the innermost stable areas and 12.3% at the edge of marsh patches experiencing a shift with consistent direction (Fig. 14c). The NDVI of the remaining 12.5% oscillates too much to allow accurate classification.

5.4. Application of multi-temporal classification mapping to salt marsh vegetation communities

Traditional long-term monitoring of salt marsh vegetation has mostly relied on field measurements, which usually require considerable sampling effort and time. Field investigations are rather challenging in vast coastal salt marsh systems like the VCR due to limited field accessibility and complex terrain. In our study, an archive of historical remote sensing images organized into flexible MNTS was proven to capture the evolution of salt marsh vegetation communities. Multi-

temporal classification maps were generated to detect spatial patterns and temporal variations of salt marsh vegetation communities, which are often difficult to obtain with *in situ* observations. However, medium spatial resolution remote sensing data like 30-m Landsat TM/ETM+ are too coarse to discriminate different salt marsh species (Frohn et al., 2012; Guttler et al., 2017). In this work, we use Landsat images to classify vegetation communities (LM, ULM, and HM) that are commonly used in salt marsh ecology (see Christian and Blum (2014)). We assume that yearly variations in peak biomass affect NDVI only to a certain extent while a change in vegetation composition is more likely responsible for a large shift in NDVI. Field measurements reported by Kirwan et al. (2012) at the VCR indicate that biomass of each salt marsh species typically varies less than 25% on a yearly basis, and this change would not lead to large shifts in NDVI (see for example Zhang et al. (1997)). The same conclusion was reached by McCaffrey and Dueser (1976), who used Landsat data to classify communities, and not to determine vegetation biomass. In future work we will explore whether vegetation biomass and the fraction of each vegetation species in each pixel can be determined from remote sensing images.

Even without a classification down at the species level, classification maps of salt marsh vegetation communities provide insight on the response of vegetation to sea level rise, because relative elevation is well represented by salt marsh vegetation. For example, ULM is likely to morph into LM when sea level rise outpaces vertical accretion. Similarly, an eroding LM is transformed in TF. Therefore, a change map of salt marsh vegetation communities (Fig. 16) not only describes vegetation succession, but also the morphological evolution of the system. Conversion of ULM to HM in the Northern part of the VCR (Fig. 16b-d) can either represent a surplus of sediment accretion against sea level rise or the encroachment of invasive species with high NDVI values. Accretion and a reduction in relative sea level allow vegetation typical of high and brackish marsh (e.g., *S. patens*, *J. roemerianus*) to encroach the LM, changing NDVI values. However, transition due to accretion

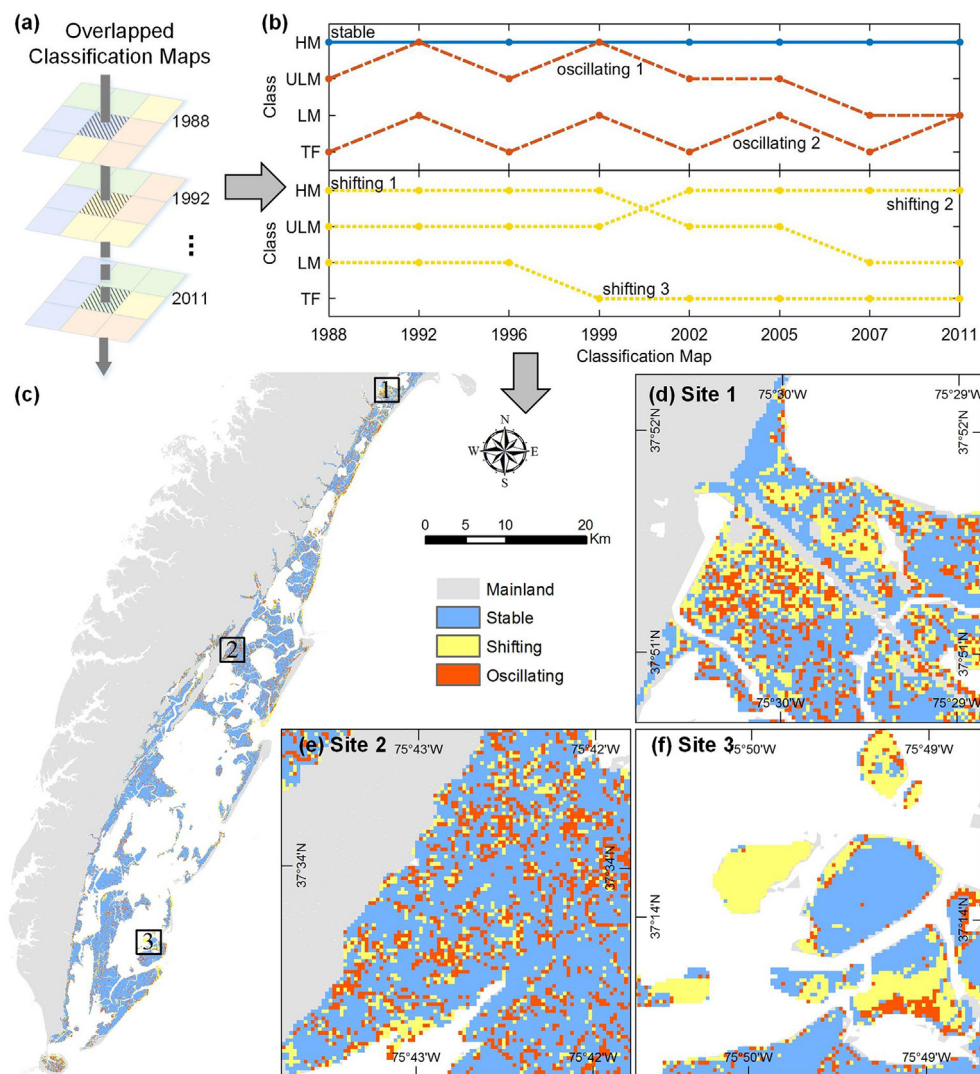


Fig. 14. Conversion patterns of salt marsh community recognized by 8 classification maps. (a) 8 classification maps overlapped by chronological order; (b) three conversion patterns (stable, shifting, and oscillating) recognized by overlapped classification maps; (c) distribution of the three conversion patterns in the VCR; (d)–(f) enlarged maps for three sites in the VCR.

seems unlikely in a period of accelerated sea level rise. Another explanation is the encroachment of invasive species occurring without an increase in bottom elevation. Encroachment of *Phragmites australis* in the ecotone between the upper limit of the salt marsh and the upland forest is well documented in this area (Bachmann et al., 2001; Chambers et al., 1999). Compared to native species, *P. australis* stabilizes surface sediments, traps suspended sediments, has a large tolerance to varying salinity and moisture regimes, and a higher ability to accumulate organic matter. Large storms, wrack deposits, and winter ice can disturb the native marsh vegetation favoring the expansion of *P. australis*. A distribution map of *P. australis* at the VCR indicated that the encroachment of this invasive species partly explains the expansion of HM at the expenses of ULM (Fig. S9 and S10 (Ngu et al., 2001)). The timing of ULM expansion is also peculiar, with high rates between 1987 and 2000 and reduced rates between 2000 and 2012 (Fig. 11b), corroborating the hypothesis that sea-level rise, and more generally, global warming, might not be the cause of this conversion.

Overall, vegetation communities typical of high elevations are replaced with vegetation communities thriving at low elevation, possibly indicating that sediment accretion is not enough to compensate sea level rise, and that on average the VCR salt marshes are becoming lower. 13.8 km² of ULM scattered across the entire VCR were converted

to LM, with a conversion rate increasing in the last 20 years. Marshes bordering open water (Fig. 16 d–g), are also susceptible to storm waves, which trigger lateral erosion (Fagherazzi et al., 2010; Fagherazzi and Wiberg, 2009). This erosion resulted in 15.1 km² of net conversions of LM to TF. Interestingly, the LM area that was lost and became TF is of the same order of the ULM area that became LM due to sea level rise (Fig. 11a). As a result, the total LM area has not changed much in the last 30 years (Fig. 11b). On the contrary, the extension of ULM dramatically decreased due to conversion to LM (likely due to an increase in sea level) and the expansion of HM (possibly due to invasive species). During 1984–2011, the total area that experienced a transformation toward habitats typical of lower elevations (37.7 km²) is twice as much as the area that experienced a conversion toward habitats with higher elevations (18.3 km²), implying a general transgressive trend for the entire VCR system.

6. Conclusions

Long-term spatial information on vegetation communities is required to understand the evolution of salt marshes and how they are affected by environmental and anthropogenic drivers. Multispectral, medium-resolution imagery can capture vegetation evolution when an

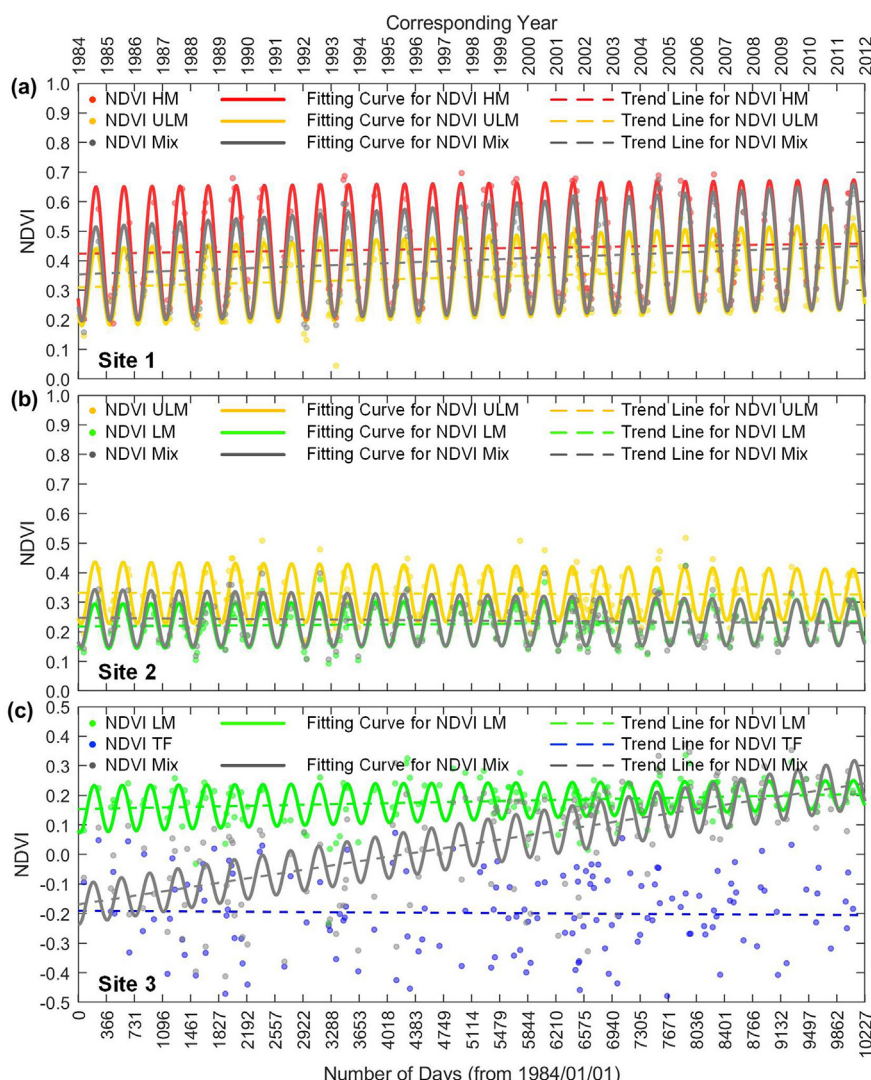


Fig. 15. NDVI time-series (1984–2011) and fitting curves for different salt marsh communities at three sites of the VCR. (a) NDVI time-series and fitting curves of ULM, HM, and their mixture at site 1; (b) NDVI time-series and fitting curves of LM, ULM, and their mixture at site 2; (c) NDVI time-series and fitting curves of TF, LM, and their mixture at site 3.

inter-annual time-series strategy is adopted, despite the limited spectral and spatial resolutions. Here we present a flexible monthly NDVI time-series (MNTS) approach based on all viable Landsat data from 1984 to 2011. The method generates multiple classification maps that allow tracking the evolution of vegetation communities in time. The general relationship between overall accuracy and average time interval between classification maps is presented. The main conclusions can be summarized as follows: (1) MNTS using Landast images are capable to accurately discriminate salt marsh vegetation communities, despite noise form clouds cover and tides. This is evidenced by the high overall accuracy of 0.898, 0.107 higher than the accuracy of a single image. (2) A significant hyperbolic relationship ($R^2 = 0.96$) exists between accuracy and average length of the time-series used for classification. This relationship allows generating long-term classification maps balancing accuracy versus number of maps. (3) The temporal evolution of salt marsh vegetation communities in the Virginia Coast Reserve is discerned from 8 classification maps spanning the period 1984–2011. The

area of Upper Low Marsh has diminished of 19.4% (15.5 km^2) with a recent accelerated trend ($R^2 = 0.92$). This area was converted either in High Marsh or Low Marsh. On average, communities lower in the tidal frame have become more common ($+37.7 \text{ km}^2$), with few areas transitioning to communities typical of higher elevations ($+18.3 \text{ km}^2$).

Acknowledgments

C.S. and Y.L. were supported by the Jiangsu Provincial Natural Science Foundation (Grant no. BK20160023), the Natural Science Foundation of China-Zhejiang Joint Fund for the Integration of Industrialization and Informatization (Grant no. U1609203). S.F. was supported by the National Science Foundation, awards NSF DEB 1237733 (VCR-LTER) and NSF OCE 1637630 (PIE-LTER). The authors are grateful to the USGS, USDA, NOAA and VCR-LTER for providing the Landsat TM/ETM + images, aerial images, LiDAR-derived DEM and water level data.

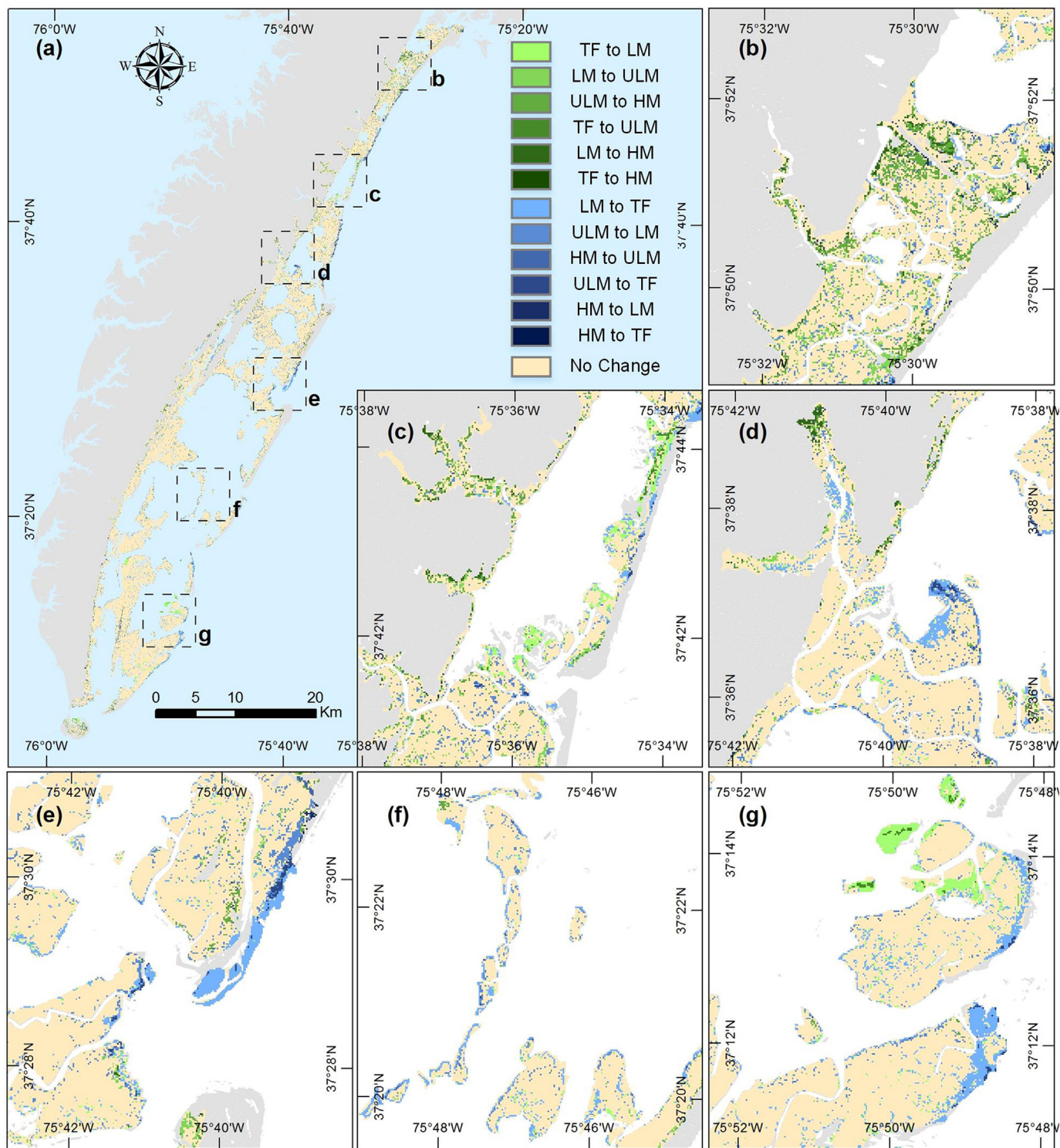


Fig. 16. Conversion map for each pair of salt marsh vegetation communities for the period 1984–2011. (a) Entire VCR system, (b)–(g) detailed conversion maps for six sites. The more dramatic change in relative elevation, the darker the color of the dash in the legend. (For interpretation of the references to color in this figure legend, the reader is referred to the Web version of this article.)

Appendix A. Supplementary data

Supplementary data related to this article can be found at <https://doi.org/10.1016/j.ecss.2018.08.007>.

Appendix B

a. C5.0 algorithm

The C5.0 algorithm was used to build a classification decision tree to map salt marsh communities. This algorithm uses the information gain ratio criterion (IGR) to determine the best attribute and candidate threshold to separate different classes (Quinlan, 1999). Specifically, the C5.0 algorithm first creates a root node of the decision tree for all samples (S). Assuming that the class field C has m different classes C_i , the information entropy for S ($IE(S)$) is calculated as:

$$IE(S) = - \sum_{i=1}^m p_i \log_2 p_i \quad (\text{A.1})$$

Where, p_i equals n_i/n , n_i and n are the number of samples for C_i and S , respectively. For the characteristic field X with non-discrete values, the C5.0 algorithm reorganizes the values to the array A_X with ascending order. If A_X has t different values, $t-1$ candidate thresholds (CT) will be generated as the averages of each two adjacent values of A_X . Each CT_j divided S into two subsets— S_{jh} with X values uniformly higher than CT_j and S_{jl} with X values uniformly lower than CT_j . The conditional information entropy when X equals CT_j ($CIE(S|X = CT_j)$) is calculated:

$$CIE(S|X = CT_j) = - \left(p_{jh} \sum_{i=1}^m p_{ijh} \log_2 p_{ijh} + p_{jl} \sum_{i=1}^m p_{ijl} \log_2 p_{ijl} \right), j = 1, 2, \dots, t-1 \quad (\text{A.2})$$

Where, p_{jh} and p_{jl} equal n_{jh}/n and n_{jl}/n . n_{jh} and n_{jl} are the number of subset S_{jh} and S_{jl} , respectively. p_{ijh} and p_{ijl} equal n_{ijh}/n_{jh} and n_{ijl}/n_{jl} . n_{ijh} and n_{ijl} are the number of C_i samples in S_{jh} and S_{jl} , respectively. Then the information gain ratio when X equals CT_j ($IGR(X = CT_j)$) and the information gain ratio for X ($IGR(X)$) are calculated as:

$$IGR(X = CT_j) = \frac{IE(S) - CIE(S|X = CT_j)}{-(p_{jh} \log_2 p_{jh} + p_{jl} \log_2 p_{jl})}, j = 1, 2, \dots, t-1 \quad (\text{A.3})$$

$$IGR(X) = \max_{j=1}^{t-1} (IGR(X = CT_j)) \quad (\text{A.4})$$

The IGR for the other characteristic fields is calculated in the same way. The root node selects the characteristic field with the largest IGR and grows two new nodes with the corresponding CT . For each new node, it repeats the above steps to generate an original decision tree until the samples of the node belongs to the same class or the number of them is lower than the minimum case specified by the user. The final tree is back-pruned from the original tree based on the reduced error pruning (EBP) algorithm with the confidence level assigned by the user (Quinlan, 1996).

b. Boosting algorithm

The main goal of the boosting algorithm is to improve classification performance through the combination of decisions from many decision trees. For each decision tree r , the boosting algorithm maintains a distribution of weights $w_r(i)$ on the training patterns i , so that each pattern can potentially have different contribution to the final training error of the decision tree. Initially, all weights are set equal; but at each iteration the weights of incorrectly classified elements are increased in order to force the decision tree to focus on these hard cases. These continuously changing weights are called adaptive weights. Once the process has finished, the single decision trees obtained are combined into a final, theoretically highly accurate decision tree based on the training data. The final decision tree therefore usually achieves a high degree of accuracy with the testing data (Bauer and Kohavi, 1999; Friedman et al., 2000). The ensemble boosting algorithm is named AdaBoost, which works according to the following mechanisms:

For a training data (TD) as:

$$TD_n = [(x_1, y_1), (x_2, y_2), \dots, (x_n, y_n)], \quad (\text{A.5})$$

with labels $y_i \in Y = [1, 2, \dots, l]$, a weight as:

$$w_r(i) = \frac{1}{n}, \quad (\text{A.6})$$

is initially assigned to every observation. These weights are recomputed according to decision tree achievements. Iteratively, for $r = 1, 2, \dots, k$, a decision tree $D_r(x)$ is trained on TD_s in order to minimize the following error:

$$E_r = \sum_{i=1}^n w_r(i) I(D_r(x_i) \neq y_i), \quad (\text{A.7})$$

where I is the indicator function, equal to one when its argument is true, zero otherwise. After r iterations the weights are initially updated:

$$w_{r+1}(i) = w_r(i) \exp(a_r I(D_r(x_i) \neq y_i)), \quad (\text{A.8})$$

$$a_r = \frac{1}{2} \ln \left(\frac{1 - e_r}{e_r} \right) \text{ and } e_r = \frac{E_r}{\sum_{i=1}^n w_i(i)}. \quad (\text{A.9})$$

After the initial update the weights are re-normalized. The final boosted decision tree is:

$$D_{\text{final}}(x) = \operatorname{argmax}_{j \in Y} \sum_{r=1}^k a_r I(D_r(x_i) = j). \quad (\text{A.10})$$

References

- Bachmann, C.M., Bettenhausen, M.H., Fusina, R.A., Donato, T.F., Russ, A.L., Burke, J.W., Lamela, G.M., Rhea, W.J., Truitt, B.R., Porter, J.H., 2003. A credit assignment approach to fusing classifiers of multisession hyperspectral imagery. *IEEE Trans. Geosci. Rem. Sens.* 41, 2488–2499.
- Bachmann, C.M., Donato, T.F., Dubois, K., Fusina, R.A., Bettenhausen, M., Porter, J.H., Truitt, B.R., 2001. Automatic Detection of an Invasive Plant Species on a Barrier Island in the Virginia Coast Reserve Using HYMAP and IKONOS Imagery. *IEEE IGARSS 2001*.
- Bauer, E., Kohavi, R., 1999. An empirical comparison of voting classification algorithms: bagging, boosting, and variants. *Mach. Learn.* 36, 105–139.
- Bellucco, E., Camuffo, M., Ferrari, S., Modenese, L., Silvestri, S., Marani, A., Marani, M., 2006. Mapping salt-marsh vegetation by multispectral and hyperspectral remote sensing. *Remote Sens. Environ.* 105, 54–67.
- Boutin, C., Keddy, P.A., 1993. A functional classification of wetland plants. *J. Veg. Sci.* 4, 591–600.
- Chambers, R.M., Meyerson, L.A., Saltonstall, K., 1999. Expansion of Phragmites australis into tidal wetlands of North America. *Aquat. Bot.* 64, 261–273.
- Christian, R., Blum, L., 2014. End of Year Biomass in Marshes of the Virginia Coast Reserve 1999–2014. knb-lter-vcr.167.21. Virginia Coast Reserve Long-Term Ecological Research Project Data Publication.
- Costanza, R., d'Arge, R., deGroot, R., Farber, S., Grasso, M., Hannon, B., Limburg, K., Naeem, S., O'Neill, R.V., Paruelo, J., Raskin, R.G., Sutton, P., vandenBelt, M., 1997. The value of the world's ecosystem services and natural capital. *Nature* 387, 253–260.
- Davranche, A., Lefebvre, G., Poulin, B., 2010. Wetland monitoring using classification trees and SPOT-5 seasonal time series. *Remote Sens. Environ.* 114, 552–562.
- de Colstoun, E.C.B., Walithall, C.L., 2006. Improving global scale land cover classifications with multi-directional POLDER data and a decision tree classifier. *Remote Sens. Environ.* 100, 474–485.
- DeFries, R., Chan, J.C.-W., 2000. Multiple criteria for evaluating machine learning algorithms for land cover classification from satellite data. *Remote Sens. Environ.* 74, 503–515.
- Esch, T., Metz, A., Marconcini, M., Keil, M., 2014. Combined use of multi-seasonal high and medium resolution satellite imagery for parcel-related mapping of cropland and grassland. *Int. J. Appl. Earth Obs. Geoinf.* 28, 230–237.
- Fagherazzi, S., Mariotti, G., Porter, J.H., McGlathery, K.J., Wiberg, P.L., 2010. Wave energy asymmetry in shallow bays. *Geophys. Res. Lett.* 37.
- Fagherazzi, S., Wiberg, P.L., 2009. Importance of wind conditions, fetch, and water levels on wave-generated shear stresses in shallow intertidal basins. *J. Geophys. Res. Earth Surf.* 114.
- Feilhauer, H., Thonfeld, F., Faude, U., He, K.S., Rocchini, D., Schmidlein, S., 2013. Assessing floristic composition with multispectral sensors—A comparison based on monoseasonal and multiseasonal field spectra. *Int. J. Appl. Earth Obs. Geoinf.* 21, 218–229.
- Fernandes, M.R., Aguiar, F.C., Silva, J.M.N., Ferreira, M.T., Pereira, J.M.C., 2013. Spectral discrimination of giant reed (*Arundo donax* L.): a seasonal study in riparian areas. *ISPRS J. Photogrammetry Remote Sens.* 80, 80–90.
- Foody, G.M., 2002a. Status of land cover classification accuracy assessment. *Remote Sens. Environ.* 80, 185–201.
- Foody, G.M., 2002b. Status of land cover classification accuracy assessment. *Remote Sens. Environ.* 80, 185–201.
- Friedman, J., Hastie, T., Tibshirani, R., 2000. Additive logistic regression: a statistical view of boosting (with discussion and a rejoinder by the authors). *Ann. Stat.* 28, 337–407.
- Frohn, R.C., D'Amico, E., Lane, G., Autrey, B., Rhodus, J., Liu, H., 2012. Multi-temporal sub-pixel Landsat ETM+ classification of isolated wetlands in Cuyahoga County, Ohio, USA. *Wetlands* 32, 289–299.
- Gao, Z.G., Zhang, L.Q., 2006. Multi-seasonal spectral characteristics analysis of coastal salt marsh vegetation in Shanghai, China. *Estuar. Coast Shelf Sci.* 69, 217–224.
- Gedan, K.B., Silliman, B.R., Bertness, M.D., 2009. Centuries of human-driven change in salt marsh ecosystems. *Annu. Rev. Mar. Sci.* 1, 117–141.
- Gilmore, M.S., Wilson, E.H., Barrett, N., Civco, D.L., Prisloe, S., Hurd, J.D., Chadwick, C., 2008. Integrating multi-temporal spectral and structural information to map wetland vegetation in a lower Connecticut River tidal marsh. *Remote Sens. Environ.* 112, 4048–4060.
- Guttler, F., Ienco, D., Nin, J., Teisseire, M., Poncelet, P., 2017. A graph-based approach to detect spatiotemporal dynamics in satellite image time series. *ISPRS J. Photogrammetry Remote Sens.* 130, 92–107.
- Harvey, K.R., Hill, G.J.E., 2001. Vegetation mapping of a tropical freshwater swamp in the Northern Territory, Australia: a comparison of aerial photography, Landsat TM and SPOT satellite imagery. *Int. J. Rem. Sens.* 22, 2911–2925.
- Isacch, J.P., Costa, C.S.B., Rodriguez-Gallego, L., Conde, D., Escapa, M., Gagliardini, D.A., Iribarne, O.O., 2006. Distribution of saltmarsh plant communities associated with environmental factors along a latitudinal gradient on the south-west Atlantic coast. *J. Biogeogr.* 33, 888–900.
- Jakimow, B., Griffiths, P., van der Linden, S., Hostert, P., 2017. Mapping pasture management in the Brazilian Amazon from dense Landsat time series. *Remote Sens. Environ.* 205, 453–468.
- Kerr, J.T., Ostrovsky, M., 2003. From space to species: ecological applications for remote sensing. *Trends Ecol. Evol.* 18, 299–305.
- Kirwan, M.L., Christian, R.R., Blum, L.K., Brinson, M.M., 2012. On the relationship between sea level and Spartina alterniflora production. *Ecosystems* 15, 140–147.
- Klemas, V., 2013. Remote sensing of emergent and submerged wetlands: an overview. *Int. J. Rem. Sens.* 34, 6286–6320.
- la Cecilia, D., Toffolon, M., Woodcock, C.E., Fagherazzi, S., 2016. Interactions between river stage and wetland vegetation detected with a Seasonality Index derived from LANDSAT images in the Apalachicola delta, Florida. *Adv. Water Resour.* 89, 10–23.
- Laba, M., Downs, R., Smith, S., Welsh, S., Neider, C., White, S., Richmond, M., Philpot, W., Baveye, P., 2008. Mapping invasive wetland plants in the Hudson River National Estuarine Research Reserve using quickbird satellite imagery. *Remote Sens. Environ.* 112, 286–300.
- Lenssen, J., Menting, F., van der Putten, W.H., Blom, K., 1999. Control of plant species richness and zonation of functional groups along a freshwater flooding gradient. *Oikos* 86, 523–534.
- Li, X., Ling, F., Foody, G.M., Ge, Y., Zhang, Y., Du, Y., 2017. Generating a series of fine spatial and temporal resolution land cover maps by fusing coarse spatial resolution remotely sensed images and fine spatial resolution land cover maps. *Remote Sens. Environ.* 196, 293–311.
- Liu, K., Shi, W., Zhang, H., 2011. A fuzzy topology-based maximum likelihood classification. *ISPRS J. Photogrammetry Remote Sens.* 66, 103–114.
- Marani, M., Bellucco, E., Ferrari, S., Silvestri, S., D'Alpaos, A., Lanzoni, S., Feola, A., Rinaldo, A., 2006. Analysis, synthesis and modelling of high-resolution observations of salt-marsh eco-geomorphological patterns in the Venice lagoon. *Estuar. Coast Shelf Sci.* 69, 414–426.
- Marceau, D.J., Howarth, P.J., Gratton, D.J., 1994. Remote sensing and the measurement of geographical entities in a forested environment. 1. The scale and spatial aggregation problem. *Remote Sens. Environ.* 49, 93–104.
- McCaffrey, C., Dueser, R., 1976. Plant Associations on the Virginia Barrier Islands: Metompkin - Smith Islands, 1974–1975. knb-lter-vcr.222.9 Virginia Coast Reserve Long-Term Ecological Research Project Data Publication.
- McCaffrey, C., Dueser, R., 1990. Plant associations on the Virginia barrier islands. *Va. J. Sci.* 41, 282–299.
- McCarthy, M.J., Halls, J.N., 2014. Habitat mapping and change assessment of coastal environments: an examination of WorldView-2, QuickBird, and IKONOS satellite imagery and airborne LiDAR for mapping barrier island habitats. *ISPRS Int. Geo-Inf.* 3, 297–325.
- Miao, X., Heaton, J.S., Zheng, S., Charlett, D.A., Liu, H., 2012. Applying tree-based ensemble algorithms to the classification of ecological zones using multi-temporal multi-source remote-sensing data. *Int. J. Rem. Sens.* 33, 1823–1849.
- Morris, J.T., Sundareshwar, P.V., Nietch, C.T., Kjerfve, B., Cahoon, D.R., 2002. Responses of coastal wetlands to rising sea level. *Ecology* 83, 2869–2877.
- Ngu, D., Albertson, J., Truitt, B., Blum, L., 2001. Phragmites Distribution in 1996 on the Eastern Shore of Virginia. knb-lter-vcr.91.16. Virginia Coast Reserve Long-Term Ecological Research Project Data Publication.
- Pengra, B.W., Johnston, C.A., Loveland, T.R., 2007. Mapping an invasive plant, Phragmites australis, in coastal wetlands using the EO-1 Hyperion hyperspectral sensor. *Remote Sens. Environ.* 108, 74–81.
- Quinlan, J.R., 1996. Bagging, Boosting, and C4.5. AAAI/IAAI, pp. 725–730.
- Quinlan, J.R., 1999. Simplifying decision trees. *Int. J. Hum. Comput. Stud.* 51, 497–510.
- Rosso, P., Ustin, S., Hastings, A., 2006. Use of lidar to study changes associated with Spartina invasion in San Francisco Bay marshes. *Remote Sens. Environ.* 100, 295–306.
- Shao, Y., Lunetta, R.S., Wheeler, B., Ilames, J.S., Campbell, J.B., 2016. An evaluation of time-series smoothing algorithms for land-cover classifications using MODIS-NDVI multi-temporal data. *Remote Sens. Environ.* 174, 258–265.
- Silvestri, S., Defina, A., Marani, M., 2005. Tidal regime, salinity and salt marsh plant zonation. *Estuar. Coast Shelf Sci.* 62, 119–130.
- Sun, C., Liu, Y.X., Zhao, S.S., Li, H.Y., Sun, J.Q., 2017. Saltmarshes response to human activities on a prograding coast revealed by a dual-scale time-series strategy. *Estuar. Coast* 40, 522–539.
- Sun, C., Liu, Y.X., Zhao, S.S., Zhou, M.X., Yang, Y.H., Li, F.X., 2016. Classification mapping and species identification of salt marshes based on a short-time interval NDVI time-series from HJ-1 optical imagery. *Int. J. Appl. Earth Obs. Geoinf.* 45, 27–41.
- Tamhane, A.C., 1977. Multiple comparisons in model I one-way ANOVA with unequal variances. *Commun. Stat. Theor. Meth.* 6, 15–32.
- Theobald, D.M., Stevens, D.L., White, D., Urquhart, N.S., Olsen, A.R., Norman, J.B., 2007. Using GIS to generate spatially balanced random survey designs for natural resource applications. *Environ. Manag.* 40, 134–146.
- Timm, B.C., McGarigal, K., 2012. Fine-scale remotely-sensed cover mapping of coastal dune and salt marsh ecosystems at Cape Cod National Seashore using Random Forests. *Remote Sens. Environ.* 127, 106–117.
- Tukey, J.W., 1949. Comparing individual means in the analysis of variance. *Biometrics* 99–114.
- Villa, P., Bresciani, M., Bolpagni, R., Pinardi, M., Giardino, C., 2015. A rule-based approach for mapping macrophyte communities using multi-temporal aquatic vegetation indices. *Remote Sens. Environ.* 171, 218–233.
- VITA, 2011. LiDAR-based Digital Elevation Model for Northampton and Accomack Co., VA, 2010. knb-lter-vcr.202.10. Reserve Long-Term Ecological Research Project Data Publication. Virginia Coast.
- Wang, L., Dronova, I., Gong, P., Yang, W.B., Li, Y.R., Liu, Q., 2012. A new time series vegetation-water index of phenological-hydrological trait across species and functional types for Poyang Lake wetland ecosystem. *Remote Sens. Environ.* 125, 49–63.
- Waske, B., Braun, M., 2009. Classifier ensembles for land cover mapping using multi-temporal SAR imagery. *ISPRS J. Photogrammetry Remote Sens.* 64, 450–457.
- Whiteside, T.G., Bartolo, R.E., 2015. Use of WorldView-2 time series to establish a wetland monitoring program for potential offsite impacts of mine site rehabilitation. *Int. J. Appl. Earth Obs. Geoinf.* 42, 24–37.
- Zedler, J.B., Kercher, S., 2005. Wetland resources: status, trends, ecosystem services, and

- restorability. *Annu. Rev. Environ. Resour.* 30, 39–74.
- Zhang, M., Ustin, S.L., Rejmankova, E., Sanderson, E.W., 1997. Monitoring Pacific coast salt marshes using remote sensing. *Ecol. Appl.* 7, 1039–1053.
- Zhao, Y., Feng, D., Yu, L., Wang, X., Chen, Y., Bai, Y., Hernández, H.J., Galleguillos, M., Estades, C., Biging, G.S., 2016. Detailed dynamic land cover mapping of Chile: accuracy improvement by integrating multi-temporal data. *Remote Sens. Environ.* 183, 170–185.
- Zhu, Z., Woodcock, C.E., 2012. Object-based cloud and cloud shadow detection in Landsat imagery. *Remote Sens. Environ.* 118, 83–94.